# Chapter 12

# Laser

Coherent light emission from lasers is considered as especially valuable because of phase information, good collimation, and high intensity.

Lasers are based on self-oscillations of light emitting systems through stimulated emission. To gain enough to overcome absorption, inversion of the quantum states is needed between which the laser transition occurs. Concentration of the emitted photons in only a few modes is obtained through forward and back reflections on mirrors. Photon emission is increased as the stimulated emission probability is proportional to the number of photons per mode.

For silicon-based photonic system different geometrical configurations of lasers are possible. The three most important ones are summarized in Table 12.1.

Often, monolithically integrated lasers on Si are considered essential for Si-based photonic systems. This is only true if a large number of light sources on a chip is required and if the cost advantages of wafer manufacturing may be realized for high-volume market segments. Nevertheless, monolithic integration of lasers on Si is considered as the "holy grail" of Si photonics as this allows the most flexible solution of complex optical sensors and communications systems. The technical goal on a long-term scale

*Silicon-Based Photonics*
Erich Kasper and Jinzhong Yu

ISBN 978-981-4303-24-8 (Hardcover), 978-1-315-15651-4 (eBook)
www.jennystanford.com

is given by monolithic integration of high-efficiency lasers where strain engineering and Sn alloy engineering of Ge on Si lasers seem to be the most promising solution paths. High efficiency of power conversion is the key for integrated lasers. Otherwise, they are unwanted hot spots on already thermally stressed chips.

**Table 12.1** Laser configurations in Si-based photonic systems

| **Laser** | Light coupling from external source | Hybrid laser mounting | Monolithically integrated laser |
|---|---|---|---|
| **Advantage** | High power, heat outside chip | High efficiency, flexibility of laser positions | Large number of lasers, wafer manufacturing |
| **Drawback** | High effort for chip housing | Hot spots on chip | Low efficiency, wavelength limitations |
| **Application potential** | Clock distribution on processor chips | Fast processor memory connections | Full system on a chip |
| **Availability** | Technical solution available | Research demonstration | First research results |

Different configurations of lasers are required for more near-term solutions and for chips with a low number of light sources.

Light coupling from external sources is an already available technical solution, which will continue to be the preferred configuration if the heat from high-power lasers is left outside the densely packed chip and if the laser light may be split and distributed around the chip dimension by a photonic waveguide network. This configuration has high application potential for optical clock distribution on processor chips. Optical clock distribution promises clear advantages beyond 10 GHz clock frequency. The topology of on optical clock is compared to an electrical clock in Table 12.2.

The optical clock needs electro-optical converters, at the source side the modulator and at the drain side the photodiode. The speed of the optical clock is limited by the electro-optical converter devices, which are now around 50 GHz fast but have the potential for more than 100 GHz speed.

**Table 12.2** Optical clock compared to an electrical clock distribution on a processor chip

| | **Electrical clock** | **Optical clock** |
|---|---|---|
| Clock source | Clock generator | Laser and modulator |
| Source-processor connection | Electrical interconnect to processor pins | Optical fiber to processor housing |
| Processor chip input | P-i-n connection to the upper level of chip metallization | Fiber output to tapered grating coupler |
| Clock signal distribution | Upper level of metallisation; RC time limited | Photonic waveguide lines and splitters |
| Transistor clock | Electrical connection from the upper level to the lower level of metallization | Electro-optical conversion by photodetectors; short-distance connection by lower-level metal lines |

## 12.1 Silicon-Based Laser Approaches

There are many different laser realizations, but in semiconductors band-to-band transitions are the preferred ones for lasers in the visible or near-infrared regime. Many direct semiconductors have proven to be excellent laser materials in diode lasers, where carrier injection is provided from forward-biased p/n junctions.

Silicon, however, is an indirect semiconductor with the lowest direct transition (more than 2 eV) above the indirect one. Occupation inversion of this high-lying direct band is practically impossible, which cancels bulk silicon from the list of diode laser materials. The optical properties of crystalline bulk silicon were shown to be modified by disorder (amorphous Si [$\alpha$-Si]), size (nanocrystal Si [nc-Si]) [1], or periodicity modulations (superlattice [SL]) [2]. Nanocrystals are rather easily produced by etching to porous silicon [3] or by annealing of Si-rich oxide [4]. Efficient room temperature visible photoluminescence from porous Si [3] and net optical gain with optical stimulation from Si nanocrystals [4] embedded in $SiO_2$ prove the successful modification of Si optical properties by size effects. These size effects are a combination of wavefunction localization, energy-level quantization, and partly binding effects on nc-Si surfaces.

In 1974, Gnutzmann and Clausecker [5] made the theoretical prediction that the imposition of a proper new periodicity in an indirect-gap semiconductor will fold the bands into a smaller Brillouin zone (BZ). This could bring the minimum of the conduction band to the $\Gamma$ point of the BZ, thus producing a quasi-direct-gap material. The band folding concept was convincingly proven with observation of folded phonons in Si/Ge superlattices using Raman spectroscopy [6]. The first experimental evidence of photoluminescence from zone-folded states of superlattices was given by Zachai et al. [7].

Electroluminescence from p-i-n diodes was obtained with the Si/Ge SL in the intrinsic part of the diode. Light emission could be demonstrated both from mesa type and waveguide devices [8].

Despite these and other exciting research results a laser could not be realized from structurally modified silicon, which switched the interest of the device- and circuit-oriented photonics community to a more practical solution path: hybrid integration of silicon photonics with the well-established group III/V laser technology [9]. As suggested in Ref. [8] two hybrid methods are preferred in terms of technology compatibility and scalability. The first one is hybrid laser integration through evanescent coupling with the photonic silicon-on-insulator (SOI) wafer. In this method a shared waveguide is created between the III/V laser and silicon. Evanescent coupling is used to deliver optical energy into the SOI photonic platform. This approach needs close proximity (<100 nm) between the III/V and Si material. This close proximity can be obtained by top-down bonding of the III/V laser on the SOI waveguide structure [10]. The other favorable approach is a special form of epitaxial transfer called transfer printing [8], because arrays of epitaxial layer coupons are collectively transferred to the receiving substrate using a specific stamp.

The success of hybrid laser integration had a large influence on the acceptance of silicon photonics but also inspired new research on monolithic integration approaches. Two monolithic approaches emerged as promising variants. The long-term approach is based on the metastable GeSn alloy that is predicted to be a direct semiconductor containing more than 10% Sn. We have dedicated a separate chapter to the GeSn alloy because of its potential importance not only for Si-based monolithic lasers but also for the shift into the mid-infrared-wavelength regime. A more near-term solution is based on the indirect semiconductor material Ge for which optically stimulated laser [11] and electrically stimulated laser operation at room temperature [12] have already been reported.

In the next section we review our basic knowledge about semiconductor lasers as obtained by more than 30 years of laser improvement in the III/V field [13–17]. The reader familiar with these principles may skip this section. Then we discuss why another indirect semiconductor (Ge) is, in contrast to Si, a reasonable candidate for laser operation and we give the status of experimental verification.

## 12.2 Basic Laser Physics

There are three main interactions that light can have with semiconductors. In an earlier chapter the absorption process of a photon has been discussed with regard to photodetectors. Figure 12.1a shows the absorption process in a schematic two-level diagram where a carrier is excited by the photon from a group state $E_0$ to an excited state $E_1$ if the photon has a frequency $v = E/h$, with $E = E_1 - E_0$.

### 12.2.1 Spontaneous Emission in a Two-Level System

For a carrier sitting in an upper energy level (Fig. 12.1b) this state is unstable. At a specific time without any external influences it will make a transition to the ground state, emitting a photon of frequency given by $hv = E_1 - E_0$ This is termed spontaneous emission and is the emission process in light-emitting diodes (LEDs). If a photon of energy $hv$ is incident on the carrier in the upper energy state $E_1$ then this photon can stimulate the emission of another photon of the same frequency and phase (i.e., it is coherent with the first photon), with the carrier making a transition to the ground state ($E_0$). This is the stimulated emission process in a laser. The radiation is monochromatic because all the photons have energy $hv$, and it is coherent because all the photons are in phase.

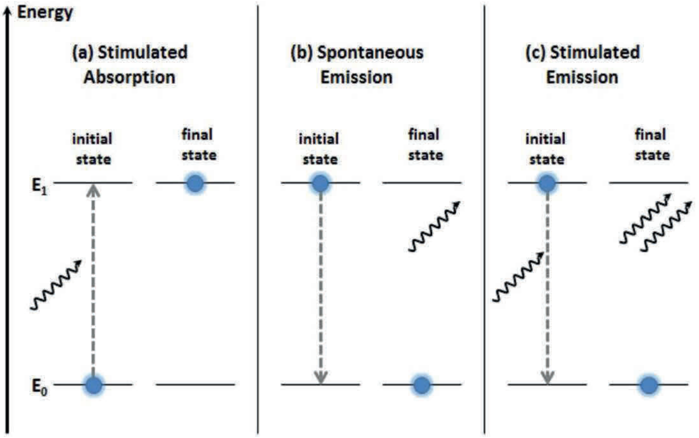

**Figure 12.1** A schematic diagram of the photonic transitions between two energy states. (a) When a carrier in the lower level absorbs a photon. (b) If a carrier is in the upper level then it can fall to the lower energy level emitting a photon with frequency $v = E/h$, where $E$ is the energy difference between the two levels. (c) If a carrier is in the upper level it can be stimulated to fall to the lower level by another photon of frequency $v = E/h$, emitting a second photon of the same frequency that is coherent (in phase) with the first photon.

Let us assume that the instantaneous populations of the states $E_0$ and $E_1$ are $n_0$ and $n_1$ respectively. Under thermal equilibrium and for $(E_1 - E_0) > 3\,k_\mathrm{B}T$ the population of the states is given by the Boltzmann distribution.

$$\frac{n_1}{n_0} = \exp\left(-\frac{E_1 - E_0}{k_\mathrm{B}T}\right) = \exp\left(-\frac{h\upsilon}{k_\mathrm{B}T}\right). \qquad (12.1)$$

As is consistent with a Boltzmann distribution, there are more carriers in the low-energy states. In the steady state, the stimulated emission rate and the spontaneous emission rate must be balanced by the rate of absorption to maintain the populations $n_0$ and $n_1$ constant.

The stimulated emission rate is proportional to the photon-field energy density in the system defined as $I(hv)$. The stimulated emission rate can, therefore, be written as $Bn_1I(hv)$. The spontaneous emission rate from $E_0$ to $E_1$ is defined as $An_1$, with $A$ a constant and independent of the photon density. $A$ and $B$ are named the Einstein coefficients. The absorption rate is proportional to the carrier population in the lower level and the photon-field energy density. Hence it is given by $Bn_0I(hv)$. In the steady state we have stimulated emission rate + spontaneous emission rate = absorption rate, that is

$$Bn_1I(hv) + An_1 = Bn_0I(hv). \tag{12.2}$$

For a laser it is stimulated emission that we are interested in dominating over spontaneous emission. Therefore, rewriting Eq. 12.2 as

$$\frac{\text{Stimulated emission rate}}{\text{Spontaneous emission rate}} = \frac{B}{A}I(h\upsilon). \tag{12.3}$$

it is clear that to enhance the stimulated emission, the photon-field density requires to be very large.

Equation 12.2 can also be rearranged to give

$$\frac{\text{Stimulated emission rate}}{\text{Absorption rate}} = \frac{n_1}{n_0}. \tag{12.4}$$

Therefore, for the stimulated emission to dominate over the absorption of photons, the upper energy state, $E_1$ requires a larger population of states than the lower energy state, $E_0$ that is, population inversion. Population inversion demands nonequilibrium caused by the injection of carriers.

## 12.3 Optical Gain in a Semiconductor

Light will be amplified in semiconductors similar to a two-level system if enough electrons are in the conduction band and enough holes in the valence band that stimulated emission overwhelm absorption. Population inversion may be obtained by absorption of a pumping laser or by injection of carriers from a forward-biased diode structure. Electrically stimulated lasers have the higher practical importance in semiconductors.

The easiest way to enhance the photon-field density is to produce a resonant optical cavity. The simplest type of cavity is a Fabry–Perot ridge waveguide (Fig. 12.2), where a ridge is etched out of the active semiconductor material. The refractive index change between the semiconductor and air is enough to reflect around 30% of the radiation at each facet.

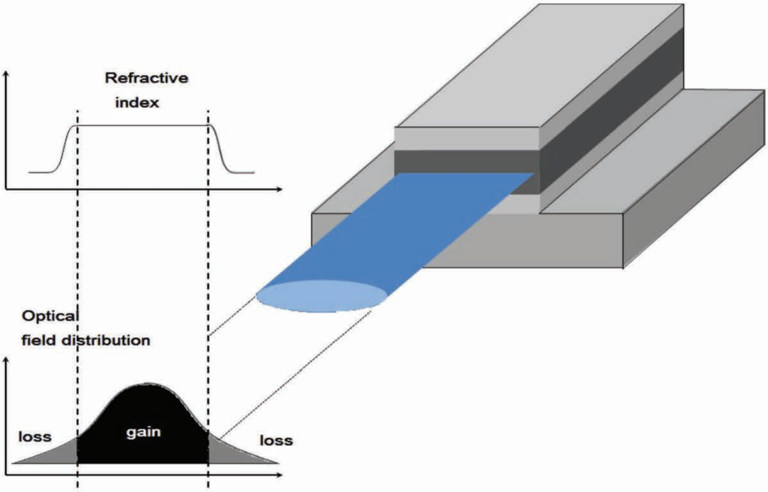

**Figure 12.2** Modal confinement into a ridge waveguide using a change in refractive index between the semiconductor and air.

Hence along the length of the cavity, standing wave modes are set up such that the frequency $\nu = kc/2L$, where $L$ is the length of the cavity, $c$ is the speed of light in the medium, and $k$ is the number describing the order of resonance. Once a cavity has been fabricated and an active semiconductor structure with population inversion has been placed in the cavity, the cavity modes (Fig. 12.3b) will convolve with the broadened electroluminescence spectrum of the transition $E_1$ to $E_0$ (Fig. 12.3a), forming the laser spectrum shown in Fig. 12.3c. This is a Fabry–Perot cavity mode spectrum, with several sharp peaks corresponding to the modes along the length of the cavity.

A diode on which a forward bias is applied shows a current that exponentially increases with applied bias voltage. The number of injected carriers increases proportionally to the current if we assume a concentration-independent lifetime of the carriers. Current has to be high enough to generate a positive net gain, which means the semiconductor gain has to overcome the losses by absorption and scattering. The current density at which lasing starts is called threshold current density $J_{\text{th}}$ (Fig. 12.4).

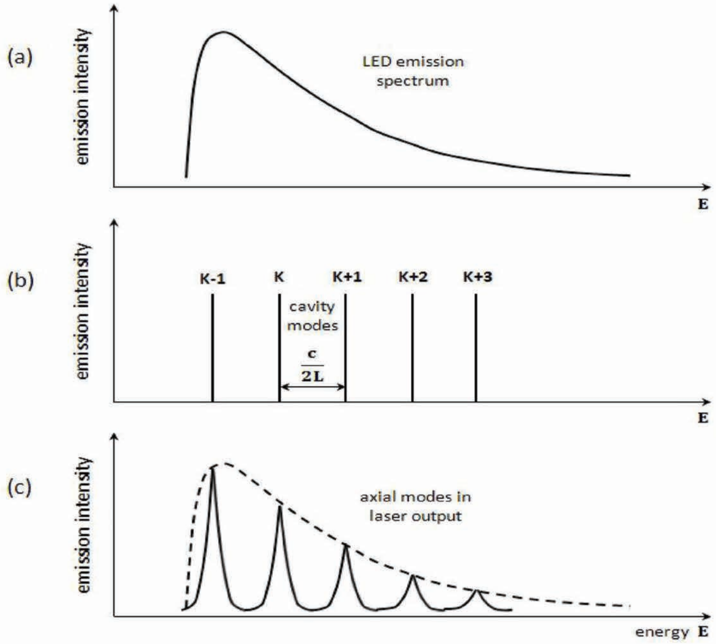

**Figure 12.3** Photoemission intensity as a function of energy. In (a) the spontaneous emission (LED) is shown. In (b) the cavity modes of a Fabry–Perot resonator are shown. In (c) the stimulated emission of a laser with axial modes from the resonator is shown.

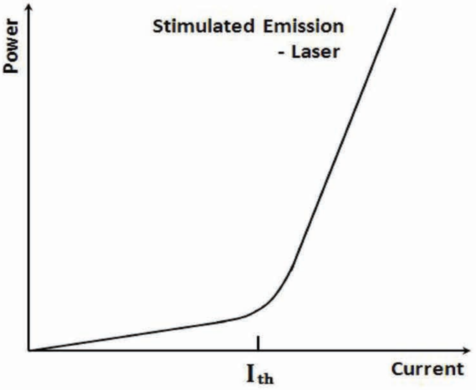

**Figure 12.4** Emission power of an electrically stimulated laser as a function of the current. Laser operation sets in from a threshold current $I_{\text{th}}$.

The energy states in semiconductors are grouped in bands. Transitions are allowed for photon energies larger than the bandgap. Semiconductors show a frequency-dependent gain spectrum if population inversion is obtained.

The principle of frequency-dependent gain is explained in the example of a semiconductor with a parabolic energy-momentum relation, which means a direct semiconductor within the effective mass model.

Figure 12.5 shows the energy states and the optical transitions in the active region of a diode laser, where carrier injection from n- and p-side increases carrier levels above equilibrium. In equilibrium the carrier occupation is described by Fermi–Dirac statistics, with a unique Fermi energy level $F$ for electrons and holes. In nonequilibrium, the carrier distribution within the bands is described again by Fermi–Dirac statistics but with separate Fermi energy levels $F_C$ and $F_V$ for the conduction band and the valence band, respectively, if intraband energy relaxation is much faster than band-to-band transitions, a situation we would assume to occur.

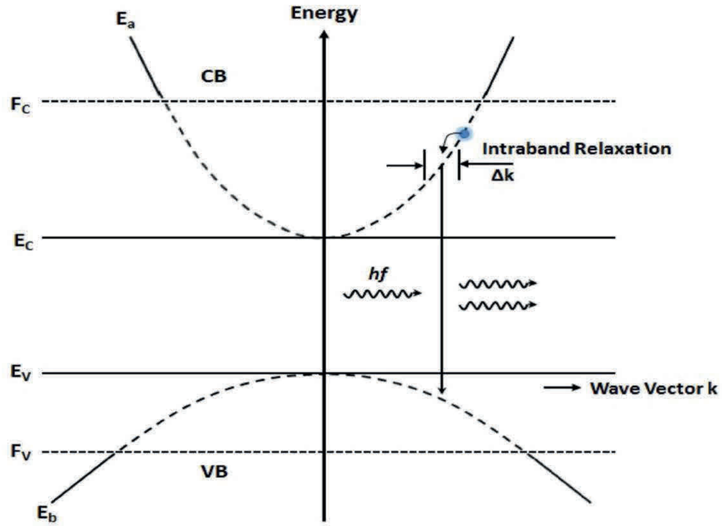

**Figure 12.5** Parabolic bandgap relation for energy $E$ versus wave vector amount $\vec{k}$ $E_c$ and $E_V$ band edges of the conduction band and the valence band. Nonequilibrium is described by different quasi-Fermi energy levels $F_c$ and $F_v$ for the both bands, respectively.

Optical transitions in the energy-momentum presentation of Fig. 12.5 are approximately vertical, which means without an essential change in momentum $\vec{k}$, because the momentum $\vec{p}$ of a photon is rather small.

We start with the gain spectrum definition for a two-level system

$$g(\nu) = \sigma(n_1 - n_0), \tag{12.5}$$

where $\sigma$ is the cross section of stimulated emission/absorption. It is easier in a semiconductor to start with a momentum-based description and then transfer to a frequency-dependent gain. The density of states (DOS) $Z(k)$ is given in a bulk semiconductor by

$$Z(k) = k^2/\pi^2, \tag{12.6}$$

which gives for $(n_1 - n_0)$ in a nonequilibrium semiconductor

$$n_1 - n_0 = \frac{k^2}{\pi^2}\Delta k(f_C - f_V), \tag{12.7}$$

with $f_C$ and $f_V$ the occupation probabilities for electrons and holes, respectively, from Fermi–Dirac statistics.

Returning to a frequency picture, we have

$$\Delta k = \frac{dk}{dE}\Delta E = \frac{dk}{d\upsilon}\Delta\upsilon \tag{12.8}$$

and

$$g(\upsilon) = \sigma(n_2 - n_1) = \sigma\frac{k^2}{\pi^2}\frac{dk}{d\upsilon}\Delta\upsilon\,(f_C - f_V). \tag{12.9}$$

The relation $dk/dv$ for parabolic bands is extracted from

$$E_a - E_C = \frac{\hbar^2 k^2}{2m_C};\ E_b - E_V = -\frac{\hbar^2 k^2}{2m_V}, \tag{12.10}$$

where the effective masses of electrons and holes are $m_C$ and $m_V$, respectively, and $E_a$ and $E_b$ are the energy levels in the conduction band and the valence band, respectively, which correspond to the transition of energy $hv$:

$$h\upsilon = E_g + \frac{\hbar^2 k^2}{2}\left(\frac{1}{m_C} + \frac{1}{m_V}\right) = E_g + \frac{\hbar^2 k^2}{2m_r}, \tag{12.11}$$

where $m_r$ is the reduced effective mass of the electron-hole pair. The optical transition probability between bands of different effective masses is proportional to $m_\mathrm{r}^{3/2}$, which is known as the joint-density-of-states model.

$$\frac{1}{m_\mathrm{r}} = \frac{1}{m_\mathrm{C}} + \frac{1}{m_\mathrm{V}} \tag{12.12}$$

Replacing $k$ by $\nu$ using the effective mass relations gives finally for the gain spectrum $g(\nu)$

$$g(\upsilon) = \frac{\sigma}{\hbar^2 \pi}(2m_\mathrm{r})^{3/2}(h\upsilon - E_\mathrm{g})^{1/2}(f_\mathrm{C} - f_\mathrm{V})\Delta\upsilon. \tag{12.13}$$

The state occupation probabilities $f_\mathrm{C}$ and $f_\mathrm{V}$ are given as

$$f_\mathrm{C} = \frac{1}{\left\{\left[\exp\frac{(E_\mathrm{a} - F_\mathrm{C})}{kT}\right] + 1\right\}} \tag{12.14}$$

and

$$f_\mathrm{V} = \frac{1}{\left\{\left[\exp\frac{(E_\mathrm{b} - F_\mathrm{V})}{kT}\right] + 1\right\}}, \tag{12.15}$$

with $F_\mathrm{C}$ and $F_\mathrm{V}$ the quasi-Fermi energy levels of a nonequilibrium semiconductor. The corresponding energy levels $E_\mathrm{a}$ and $E_\mathrm{b}$ in conduction and valence bands may be expressed as a function of the photon energy $h\nu$:

$$E_\mathrm{a} = (h\upsilon - E_\mathrm{g})\frac{m_\mathrm{r}}{m_\mathrm{C}} + E_\mathrm{C} \tag{12.16}$$

$$E_\mathrm{b} = (h\upsilon - E_\mathrm{g})\frac{m_\mathrm{r}}{m_\mathrm{V}} + E_\mathrm{V} \tag{12.17}$$

## 12.4 Semiconductor Heterostructure Laser

In our basic consideration of the laser operation a p-i-n diode junction was used for injection of the high current that allows inversion of the quantum states. This means that one has to fill the conduction band states at least a few $kT$. The development of direct bandgap lasers from III/V material demonstrated that band filling could be effectively obtained by carrier confinement in semiconductor heterostructures [13]. A material sequence ABA, where material B has a lower energy for carriers than material A, is called a double heterostructure (DH), which collects the injected carriers within the material slab B. The DOS $Z(E)$ for these collected carriers is bulk like (3D movement) if the thickness $d$ of the slab B is on the order of the intrinsic region of the doping structure (typically 150 nm). Note that the DOS is usually given as a function of energy $E$. The momentum-based DOS $Z(\mathrm{k})$ of Eq. 12.6 may be transferred to $Z(E)$ by using Eq. 12.8. Quantum size effects [14] will have a considerable influence on the DOS (Fig. 12.6) if the thickness $d$ shrinks to several tens of nanometers. The structure is called quantum film or quantum well (QW) if the carrier confinement is in one direction (2D movement), and it is called quantum wire or quantum box if confinement is performed in two directions (1D movement) or all three directions (0D movement), respectively. A scheme [15] of the quantum size structures and their DOS $Z(E)$ is given in Fig. 12.6. A DH laser and a QW laser differ only in their thickness $d$, which changes not only the DOS but also the optical confinement.

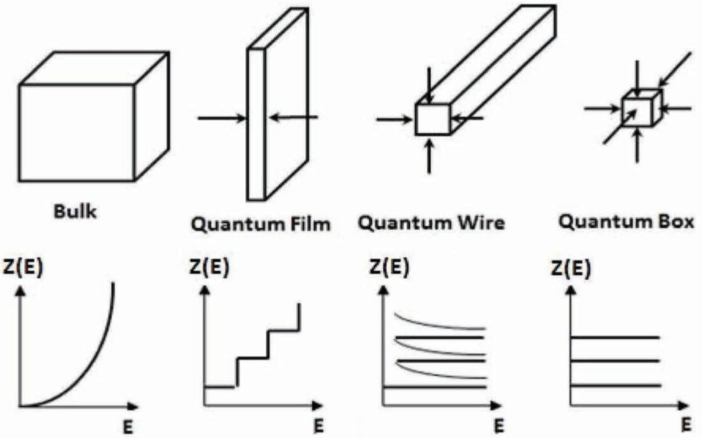

**Figure 12.6** Schematics of 3D, 2D, 1D, and 0D quantum systems and corresponding densities of states Z(E). Graph compiled using data from Ref. [15].

The wavelength of the infrared light is only about several hundred nanometers in a semiconductor because of the high refractive index $n$. The thickness $d$ of a DH laser is comparable with the wavelength of light; in contrast the thickness of QW is much smaller than the wavelength. This is discussed later, under optical confinement factor.

A main parameter is the optical confinement factor Γ, which represents the fraction of the optical wave in the active layer material, that is, the efficiency of an emitted photon to interact with another electron-hole pair in order to further induce stimulated emission. This confinement factor depends on the active layer thickness and on the difference in the indexes of refraction between the active layer and confining materials.

$$\Gamma = \frac{\int_{-d/2}^{+d/2} |E(z)|^2 \, dz}{\int_{-\infty}^{+\infty} |E(z)|^2 \, dz} \tag{12.18}$$

As indicated in Fig. 12.7, the $d^2$ variation of Γ for simple heterostructures [13] leads to extremely small values of Γ in QWs, typically $4 \cdot 10^{-3}$ for $d = 10$ nm. Using the separate-confinement heterostructure (SCH) scheme, with a fixed cavity to confine the optical wave separately from the electron wave (QW), one obtains $\Gamma \approx 3 \cdot 10^{-2}$ in a 10 nm GaAs/GaAlAs QW. Note that the width of the single quantum well (SQW) as the confining waveguide is too thin whereas in the SCH case, the optical waveform is independent of the QW thickness as it is confined by the intermediate composition layer.

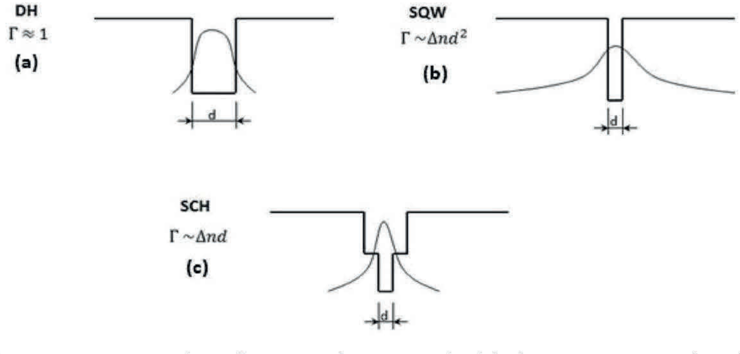

**Figure 12.7** Optical confinement factors in double heterostructures (DHs). Schematics of conduction band edge and corresponding optical wave for a DH (a), a single quantum well (SQW) (b), and a separate-confinement heterostructure (SCH) (c).

The gain $g_{\mathrm{th}}$ at the threshold is obtained by stating that the optical wave intensity after a roundtrip in the cavity must stay equal under the opposite actions of losses and gain. This is conveniently written as:

$$I_0 R^2 e^2(\Gamma g_{\mathrm{th}} - \alpha)L = I_0, \qquad (12.19)$$

where $R$ is the facet reflectivity; $L$ is the laser length; $\Gamma g_{\mathrm{th}}$ represents the modal gain per unit length of the optical wave; and $\alpha$ sums all the various loss mechanisms, such as free carrier absorption, light scattering by waveguide imperfections, and barrier material absorption, but not the fundamental absorption of the active layer, which is already included in the gain $g$ definition. Equation 12.19 can be rewritten in the form:

$$\Gamma g_{\mathrm{th}} = \alpha + \frac{1}{L}\ln\frac{1}{R} \qquad (12.20)$$

In GaAs/GaAlAs lasers, the first term is usually 10 $\mathrm{cm}^{-1}$ and the second 40 $\mathrm{cm}^{-1}$ for a 300 μ long laser and uncoated facet reflectivity of 0.3.

The threshold current is known once the gain versus injected current is determined. This can be readily done by using the carrier density as an input parameter. For that density one can calculate both the maximum gain and the required injection current from the known radiative and nonradiative recombination channels. As mentioned above, gain occurs only once significant inversion has been achieved.

Confinement of carriers in 2D structures as the main measure to obtain high carrier densities turned out to be a convenient way to reduce the required threshold current density. Several variants of QWs were developed to also meet the requirements of optical confinement.

- SQW: Each quantized well state introduces a 2D DOS equal to $m * \hbar^2$, while the onset of 3D states at the top of the well introduces a much larger DOS.
- Multiple quantum well: Each quantized state introduces a 2D DOS equal to $Nm * \hbar^2$, $N$ being the number of wells.
- SCH laser: The intermediate-composition layers that surround the inner well introduce a large DOS, not as far apart from the ground state as in the DH, SQW, or multiple quantum well (MQW) cases.

- Graded-index SCH laser: The QW is surrounded by a region with steadily increasing refractive index. A ladder of quantum states in the graded region is added to the states of the inner well.

As discussed above, the SQW structure leads to $\Gamma \approx 4 \cdot 10^{-3}$, an unacceptable value, and one has to resort to the various structures shown in Fig. 12.8 [16, 17].

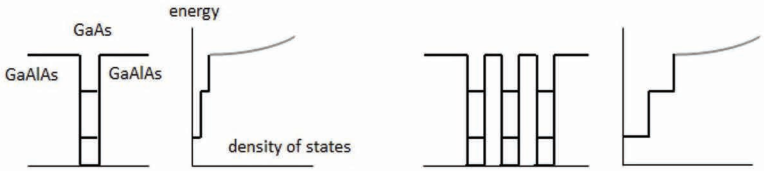

**Single Quantum Well**
**(A)**

**Multiple Quantum Well**
**(B)**

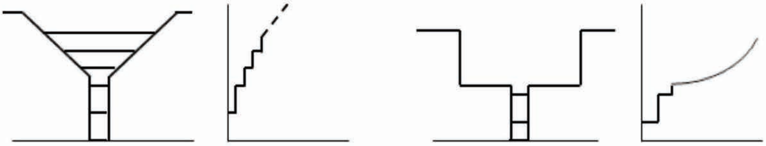

**GRIN-SCH-Quantum Well**
**(C)**

**SCH-Quantum Well**
**(D)**

**Figure 12.8** Various quantum well laser structures schematically depicted by their conduction band edge space variations (the left one in each set of figures) and their 2D density of states *Z*(*E*) (right side).

## 12.5 Conduction Band Occupation in an Indirect Semiconductor

The indirect conduction band in an indirect semiconductor is occupied by more electrons than the direct one under equilibrium as a result of the Fermi–Dirac statistics. This general law of statistics can only be overcome with very fast transients, for example, injection of carriers at energies above the direct gap. The corresponding time frame is given by the lifetime of intervalley scattering, which is on the order of a few hundred femto seconds. The lifetime of the direct ($\Gamma$) – indirect ($L$) intervalley electron scattering in bulk Ge [18, 19] and

Ge/SiGe QWs is reported to be 230 fs and 185 fs [20], respectively. The high occupation of the direct transition was demonstrated in a femto second spectroscopy [21], with optical excitation leading to an optical gain (1300 $\text{cm}^{-1}$) comparable with direct semiconductors and 25 times larger than the steady-state gain. These results could pave the way to pulsed laser operation of indirect semiconductors with high efficiency.

### 12.5.1 Steady-State Occupation Model for Indirect Semiconductors

In the following parts we will assume Fermi–Dirac statistics for the conduction band and the valence band, with quasi-Fermi energy levels $F_\text{c}$ and $F_\text{v}$ in the injection regime.

For a simple model of the occupation statistics influence let us assume the same effective mass for the direct and indirect conduction bands. For low injection the Boltzmann approximation is valid. The ratio $n_\text{dir}/n_\text{ind}$ of direct to indirect occupation is then simply given by Eq. 12.21:

$$\frac{n_\text{dir}}{n_\text{ind}} = \exp\left(-\frac{\Delta E}{k_\text{B}T}\right), \tag{12.21}$$

with $\Delta E$ the energy difference between the indirect and direct conduction bands. In Si the difference $\Delta E$ is very high (more than 2 eV) and the ratio $n_\text{dir}/n_\text{ind}$ negligible (about $10^{-35}$), so the upper level can be considered to be unoccupied. In Ge this energy difference shrinks to 0.136 eV or even lower for tensile-strained Ge. Then the upper level is also partly occupied and the ratio is small, for example, $5 \cdot 10^{-3}$ at room temperature and the simplifications made in Eq. 12.21. But even with this small ratio of below 1% direct transition dominates light emission because of the much higher radiative transition efficiency.

At medium and higher injection levels the ratio $n_\text{dir}/n_\text{ind}$ increases above the fixed value (Eq. 12.21) of the Boltzmann approximation. This increase of the ratio $n_\text{dir}/n_\text{ind}$ starts when the quasi-Fermi level $F_\text{c}$ enters the indirect conduction band ($F_\text{c} - E_\text{cind} > 0$). It follows from simple mathematical properties of the modified Fermi–Dirac integral $F_{1/2}$, which describes the carrier density from folding of DOS with Fermi–Dirac statistics in bulk (3D) materials.

$$n = N_c F_{1/2}\left((F_c - E_c)/kT\right) \qquad (12.22)$$

The effective DOS $N_c$ is given by

$$N_c = \left(\frac{2\pi m^* kT}{h^2}\right)^{3/2} M_c, \qquad (12.23)$$

with $M_c$ as the number of equivalent minima (degeneracy of the band edge). The Fermi integral $F_{1/2}$ increase in the Boltzmann approximation regime as

$$F_{1/2}((F_c - E_c/kT)) = \exp((F_c - E_c)/kT), \qquad (12.24)$$

where

$$(F_c - E_c)/kT < 0,$$

but for positive values of $(F_c - E_c)/kT$ the slope is smaller than for an exponential curve.

The modified Fermi–Dirac integral $F_{1/2}$ is normalized by a near unity prefactor ($2\sqrt{\pi} = 1.128$) to get exactly the exponential function for the Boltzmann approximation regime (Eq. 12.22).

The definition of the modified Fermi–Dirac integral of the order ½ is given by [22]

$$F_{1/2}(x) = \frac{2}{\sqrt{\pi}} \int_0^\infty \frac{u^{1/2}}{1 + \exp(u - x)} du. \qquad (12.25)$$

(Please note that the Fermi–Dirac integral is sometimes used without the prefactor, for example, in the popular book in Ref. [23]. The prefactor has then to be added to the relation 12.22).

The deviation of $F_{1/2}(x)$ from $\exp(x)$ is clearly visible at positive values of the argument $x$ as shown in Table 12.3, which lists the ratio $R$ between exponential function and modified Fermi–Dirac integral.

$$R = \frac{\exp(x)}{F_{1/2}(x)} \qquad (12.26)$$

The connection to statistics is obvious if one uses the substitution given in Eq. 12.27.

$$\chi = (F_c - E_c)/kT \qquad (12.27)$$

The deviation from Boltzmann approximation ($R > 1$) increases strongly with the quasi-Fermi level entering the conduction band, with $R$ already reaching a value of 16.8 at $(F_c - E_c) = 5$ kT (around 125 meV at room temperature).

**Table 12.3** The ratio $R$ is tabulated for the range from Boltzmann approximation ($x < 0$) to positive values of $x$

| $x$ | −4 | −3 | −2 | −1 | 0 | 1 | 2 | 3 | 4 | 5 |
|---|---|---|---|---|---|---|---|---|---|---|
| $R$ | 1.00 | 1.02 | 1.05 | 1.12 | 1.31 | 1.72 | 2.62 | 4.5 | 8.4 | 16.8 |

The same relation (Eq. 12.26) holds for the hole quasi-Fermi energy $F_\mathrm{v}$ in the valence band but with an inverted energy scale.

$$x = \frac{E_v - F_v}{kT} \tag{12.28}$$

For the simple model with the same effective direct/indirect masses an approximation [24] is given for quasi-Fermi energies above the indirect band edge but below the direct band edge.

$$\ln\left(\frac{n_\mathrm{dir}}{n_\mathrm{ind}}\right) = -\frac{\Delta E_\mathrm{C}}{kT} + \left(\frac{3}{4}\sqrt{\pi}\right)^{2/3}\left(\frac{n_\mathrm{ind}}{N_\mathrm{c}}\right)^{2/3} - \ln\left(\frac{n_\mathrm{ind}}{N_\mathrm{c}}\right), \tag{12.29}$$

where

$$\left(\frac{n_\mathrm{ind}}{N_\mathrm{c}}\right) > 1 \text{ and } \left(\frac{n_\mathrm{dir}}{N_\mathrm{c}}\right) < 1.$$

The first term of Eq. 12.27 describes the Boltzmann approximation, and the second and third terms describe the influence of the Fermi integral $F_{1/2}$ on the occupation statistics of the indirect conduction band. The value of the ratio $\frac{n_\mathrm{dir}}{n_\mathrm{ind}}$ in Eq. 12.29 is plotted in Fig. 12.9 as a function of the relative indirect electron concentration $\left(\frac{n_\mathrm{ind}}{N_\mathrm{c}}\right)$ in a double logarithmic presentation.

This is done on a simplified (same effective mass direct and indirect electrons) hypothetical two-band system to demonstrate the influence of Fermi–Dirac statistics. The higher the electron density, the higher is the ratio of direct electrons to indirect electrons, which means that radiative recombination from direct states increases superlinearly with electron concentration. This simple outcome from general Fermi–Dirac statistics plays an important role in the design of indirect semiconductor lasers, which benefits from a larger ratio of direct-to-indirect transitions. This variable ratio of direct-to-indirect states is popularly described as the quasi-direct character of the highly n doped indirect semiconductor. However, the number of direct electrons is always lower than the indirect ones, although the ratio improves when the Fermi energy enters the conduction band.

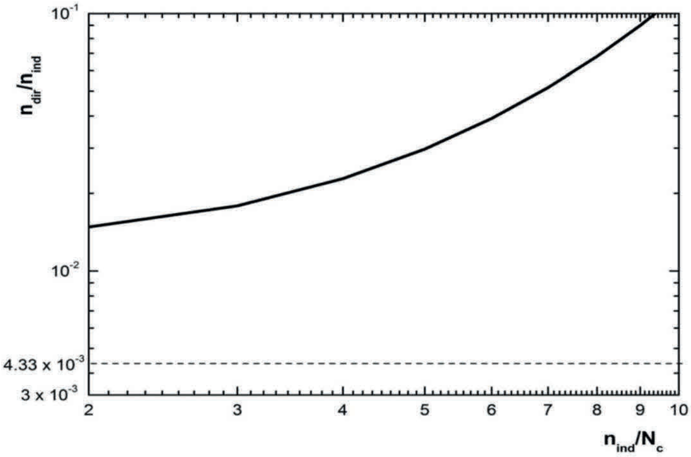

**Figure 12.9** Presentation of the ratio $\left(\frac{n_{\text{dir}}}{n_{\text{ind}}}\right)$ versus relative electron concentration $\left(\frac{n_{\text{ind}}}{N_{\text{c}}}\right)$ in a double logarithmic plot. Assumed are same effective masses for direct and indirect electrons of a hypothetical indirect semiconductor with $\Delta E_{\text{c}}$ = 136 meV.

## 12.5.2 Effective Density of State for Ge

The band edge of the band structure may be described by the parabolic dependence of the energy $E$ on the wave number because a steady function $E(k)$ has no linear term at the extrema points. The effective mass is then given by

$$\frac{\partial^2 E}{\partial k^2} = \frac{\hbar^2}{m^*}. \tag{12.30}$$

An effective mass independent from the direction is typical for the direct conduction band state, which means a spherical constant energy surface in the $E(k_x, k_y, k_z)$ representation. For the indirect transition the $E(\vec{k})$ relation near the maximum energy is written as

$$E - E_{\text{cind}} = \frac{\hbar^2}{2}\left(\frac{(k_{\text{c}} - k_0)^2}{m_{\text{e}}} + \frac{{k_{\text{t}}}^2}{m_{\text{t}}}\right), \tag{12.31}$$

which may be presented by an ellipsoidal constant energy surface. The direction toward the minimum energy shows the longitudinal effective mass $m_e$. Both transversal directions have a different transverse effective mass $m_t$. The mean value for the effective DOS calculations is the DOS effective mass $m^*_{\mathrm{DOS}}$, which is written in this chapter as $m^*$ as we do not need any other mean value calculation (e.g., for conductivity)

$$m^* = (m_e{}^* m_t{}^2)^{3/2} \tag{12.32}$$

In the valence band the extremum of the energy (maximum) is always direct at $k = 0$. Two sub-bands, heavy hole (hh) and light hole (lh), are degenerate at the BZ center. The band curvature $\frac{\partial^2 \mathrm{E}}{\partial k^2}$ is not isotropic for the direct valence band but is given by a nonisotropic [25] energy wave number function $E(k)$

$$\frac{2m_0}{\hbar^2}(E_{\mathrm{v}} - E) = Ak^2 \pm \left[B^2k^4 + C^2\left(k_{\mathrm{x}}{}^2k_{\mathrm{y}}{}^2 + k_{\mathrm{y}}{}^2k_{\mathrm{z}}{}^2 + k_{\mathrm{z}}{}^2k_{\mathrm{x}}{}^2\right)\right]^{1/2} \tag{12.33}$$

The plus/minus sign in Eq. 12.33 is valid for the hh/lh sub-bands. The valence band parameters *A*, *B*, and *C* are given in Table 12.4 [25].

**Table 12.4** Valence band parameters *A*, *B*, and *C* for Ge (in comparison with Si) (compiled from data given in Ref. [25])

| | A | B | C | SOED |
|---|---|---|---|---|
| Ge | −13.3 | −8.6 | 12.8 | 290 meV |
| Si | −4.3 | −0.6 | 4.9 | 44 meV |

*Note*: Spin-orbit energy difference (SOED) for the split-off band is added to show the rather high energy difference for Ge.

Along the cubic axes the effective masses are $\frac{m_0}{A+B}$ and $\frac{m_0}{A-B}$ for the light holes and the heavy holes, respectively. A third sub-band, the spin-orbit split-off band, need not usually be considered for occupation statistics in Ge because of the rather large energy separation SOED of 290 meV. The effective DOSs for the different sub-bands were calculated with the use of Eq. 12.23. The number of equivalent minima $M_c$ for the indirect band is 4, and for all other sub-bands $M = 1$ was chosen. The values of the effective masses differ slightly in literature because of experimental uncertainty and deviations from parabolicity of the band structure. We have chosen here the values selected in Ref. [23].

The effective masses and the calculated effective DOS for the four sub-bands (in the conduction band indirect and direct sub-bands with subscripts ind and dir, respectively. In valence band heavy hole and light hole sub-bands with subscripts hh and lh, respectively) are summarized in the Table 12.5.

**Table 12.5** The effective masses $m^*$ of the Ge conduction and valence sub-bands in units of the free electron mass $m_o$

| **Band** | **Conduction** | | **Valence** | |
|---|---|---|---|---|
| Sub-band | ind | dir | hh | lh |
| $m^*/m_o$ | 0.22 | 0.038 | 0.28 | 0.044 |
| $N_c/N_v$ (units $10^{18}$ cm$^3$) | 10.75 | 0.185 | 3.7 | 0.23 |

*Note*: The subscripts ind, dir, hh, and lh refer to the indirect and direct conduction sub-bands and heavy hole and light hole valence sub-bands. The corresponding effective densities of states are calculated from Eq. 12.23.

The effective DOS of a nominal band with free electron mass $m_o$ is given as 2.5 × $10^{19}/\text{cm}^3$. The effective DOS of the different Ge sub-bands varies considerably from the $10^{17}/\text{cm}^3$ range (dir, lh) to the $10^{18}/\text{cm}^3$ range (hh) and the onset of the $10^{19}/\text{cm}^3$ range (ind). The effective density of the band is the weighted sum of the sub-band densities within the Boltzmann approximation.

$$N_c = N_{\text{cind}} + N_{\text{cdir}}{}^*\exp\left(\frac{-\Delta E_c}{kT}\right) \tag{12.34}$$

The much higher density $N_{\text{cind}}$ of the indirect band and the energy distance $E_c$ of the direct band allow the contribution of the direct band to be rather low (about $10^{-4}$) so that $N_c = N_{\text{cind.}}$ This holds true even up to the indirect/direct crossover $\Delta E_c = 0$, which can be obtained with very high tensile strain or Sn alloying.

For the valence band of an unstrained group IV semiconductor we obtain

$$N_v = N_{\text{vhh}} + N_{\text{vlh}}. \tag{12.35}$$

The valence band degeneracy at $\vec{k} = 0$ is lifted by an applied strain. Under tensile strain the lh sub-band is the higher lying. Then we obtain with an energy difference $\delta E_\mathrm{v}$ between both sub-bands hh and lh

$$N_\mathrm{v} = N_\mathrm{vlh} + N_\mathrm{vhh} {}^{*}\exp(-\delta E_\mathrm{v}). \tag{12.36}$$

At the valence band we see a much lower density from the lh sub-bands (0.23 versus $3.7 \cdot 10^{-18}/\mathrm{cm}^3$ for the hh band) so that the density $N_\mathrm{v} = 4 \cdot 10^{-18}/\mathrm{cm}^3$ is mainly determined by the hh sub-band. Tensile strain reduces the density $N_\mathrm{v}$ by lowering the weight of the density $N_\mathrm{vhh}$ (Eq. 12.36). However, an energy difference of the sub-bands of $3k_\mathrm{B}T$ (75 meV at room temperature) is necessary for a reduction of $N_\mathrm{v}$ toward the $N_\mathrm{vlh}$.

A definition of a common DOS for nondegenerate sub-bands with an energy difference $\Delta E$ is not possible outside the Boltzmann approximation. Then the carrier density $n$ (or $p$) has to be written as the sum of both sub-bands.

$$n = N_{c1}F_{1/2}(x) + N_{c2}F_{1/2}(x - \Delta x), \tag{12.37}$$

with the abbreviations $x = (F_\mathrm{c} - E_\mathrm{c})/kT$, $\Delta x = \Delta E/kT$.

The following Table 12.6 gives a comparison of the Fermi–Dirac integral $F$ (order ½) with the Boltzmann approximation.

**Table 12.6** Fermi–Dirac integral $F_{1/2}$ in comparison with the exponential functions exp($x$)

| $x = (F_\mathrm{c} - E_\mathrm{c})/kT$ | $F_{1/2}(x)$ | Exp($x$) |
|---|---|---|
| –4 | $1.8 \cdot 10^{-2}$ | $1.8 \cdot 10^{-2}$ |
| –3 | $4.9 \cdot 10^{-2}$ | $5 \cdot 10^{-2}$ |
| –2 | $12.9 \cdot 10^{-2}$ | $13.5 \cdot 10^{-2}$ |
| –1 | $32.8 \cdot 10^{-2}$ | $36.8 \cdot 10^{-2}$ |
| 0 | $76.5 \cdot 10^{-2}$ | 1 |
| 1 | 1.58 | 2.71 |
| 2 | 2.82 | 7.38 |
| 3 | 4.49 | 20.1 |
| 4 | 6.51 | 54.6 |
| 5 | 8.84 | 148.4 |

Many rather accurate approximations of the Fermi–Direct integral are available. A rather easy intrinsic form is suggested by Kroemer [26] for arguments $x > 1$.

$$x = \ln(F_{1/2}(x)) + 0.35\, F_{1/2}(x) \qquad (12.38)$$

The rather simple Kroemer approximation (Eq. 12.38) is accurate enough to be used together with the effective mass approximation because both are very good for Fermi energies near the band edges and both lose some accuracy at higher Fermi energies but are good to predict systematic trends. For higher numerical accuracies the full band structure has to be considered.

## 12.6 Influence of Strain and Sn Alloying

A necessary condition for an active material in a semiconductor laser is the population inversion that starts when the quasi-Fermi energies $F_C$ and $F_V$ enter the conduction band and the valence band, respectively. Then the gain $g$ (Eq. 12.5) switches from a negative value (stimulated absorption dominates) to a positive value (stimulated emission dominates). In a real-world laser the gain at threshold $g_{th}$ (Eq. 12.20) has to be larger than zero in order to counterbalance modal losses (described by the confinement factor Γ) and extinction losses (described by the coefficient $\alpha'$). Modal losses and extinction losses depend on the dedicated device structure, so that we follow in the fundamental material discussion the necessary condition $g = 0$. Next, we consider an n-doped active device in which a nonequilibrium carrier density is injected. In the active material region the total carrier density is then given as

$$\text{Electrons} \quad n = N_d + \Delta n$$

and

$$\text{Holes} \quad p = \Delta p.$$

The higher electron charge $-qn$ is counterbalanced by the lower charge $+ q\mathrm{N}_D$ and the hole charge $+ q\Delta p$. For the calculation of the Fermi energy levels $F_C$ and $F_V$ in a two-sub-band system Eqs. 12.36 and 12.37 may be used. We obtain for the Fermi energy touching the direct conduction band the relation:

$$N_d + \Delta n = N_{ind} F_{1/2}(\Delta X_c) + N_{dir} F_{1/2}(0) \qquad (12.39)$$

For the strain-split valence band we obtain Eqs. 12.40 and 12.41, respectively.

$$\Delta p = N_{\mathrm{vlh}} F_{1/2}(0) + N_{\mathrm{vhh}} F_{1/2}(\delta X_{\mathrm{v}}) \tag{12.40}$$

Equation 12.40 is valid for tensile strain when the lh band is on top.

$$\Delta p = N_{\mathrm{vhh}} F_{1/2}(0) + N_{\mathrm{vlh}} F_{1/2}(\delta X_{\mathrm{v}}) \tag{12.41}$$

Equation 12.41 is valid for compressive strain when the hh band is on top.

For clarity of presentation we use for the band parameters $N_{\mathrm{V}}$ and $N_{\mathrm{C}}$ the same values as for unstrained Ge. These values are given in Table 12.5. Let us explain the treatment for strained Ge where the normalized quantities are defined as

$$\Delta X_{\mathrm{c}} = \frac{E_{\mathrm{cind}} - E_{\mathrm{cdir}}}{k_{\mathrm{B}} T} \tag{12.42}$$

and

$$\delta X_{\mathrm{v}} = \frac{E_{\mathrm{Vlh}} - E_{\mathrm{Vhh}}}{k_{\mathrm{B}} T}. \tag{12.43}$$

At room temperature unstrained Ge has

$$\Delta X_{\mathrm{c}} = 136\ \mathrm{meV}/25\ \mathrm{meV} = 5.44$$

and

$$\Delta X_{\mathrm{v}} = 0.$$

Using the values of Tables 12.5 and 12.6 one obtains $p = \Delta p = 3 \times 10^{18}/\mathrm{cm}^3$ and $n = N_{\mathrm{d}} + \Delta n = 1 \times 10^{20}/\mathrm{cm}^3$. The necessary condition $g = 0$ will be obtained at room temperature in unstrained Ge with a very high n-doping ($10^{20}/\mathrm{cm}^3$) and a moderate injection density level of $\Delta p = \Delta n = 3 \times 10^{18}/\mathrm{cm}^3$.

The very high n-doping is problematic both for technological reasons as well as for increasing the free carrier absorption and reducing the carrier lifetime by Auger recombination. The need for very high n-doping may be reduced effectively by smaller values of the direct-indirect bandgap energy $\Delta E_{\mathrm{c}}$. This energy difference shrinks with larger lattice spacing, which may be obtained by tensile strain or alloying with a larger atom like Sn (or maybe with the even larger Pb atom in the future).

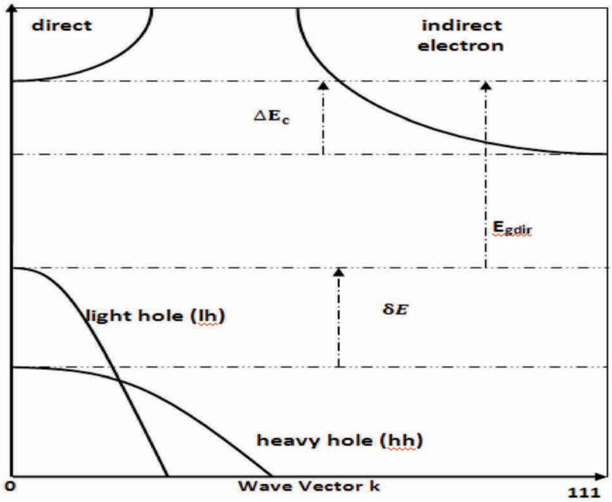

**Figure 12.10** Band structure of tensile-strained Ge (biaxial stress). The essential quantities for laser operation are the energy difference $\Delta E_c$ between indirect and direct conduction bands, the direct bandgap $E_{gdir}$, and the energy splitting $\delta E$ between heavy hole and light hole band. The bandgap $E_{gdir}$ is not shown to scale.

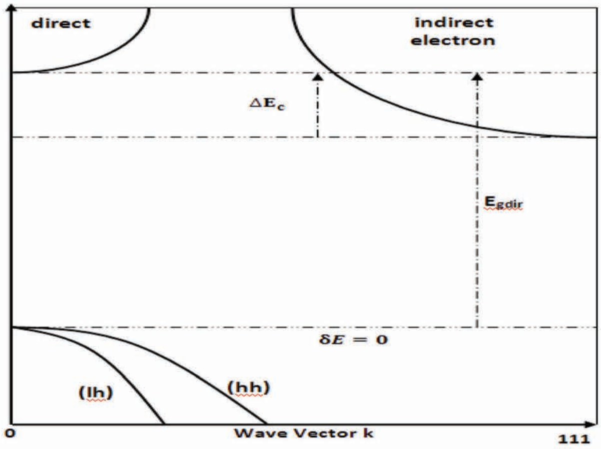

**Figure 12.11** Band structure of unstrained GeSn.

The much higher effective DOS of the indirect band (roughly 50 times higher than that of the direct one, see Table 12.5) dominates the carrier density not only in the indirect semiconductor region

($\Delta E_c > 0$) but also at the crossover ($\Delta E_c = 0$) till deep into a direct semiconductor ($\Delta E_c = -4k_BT$) behavior. At crossover the necessary electron density is about $1.1\cdot10^{19}/\text{cm}^3$, and it drops to about $3\times10^{17}/\text{cm}^3$ at a direct semiconductor with $\Delta E_c = -100$ meV. The valence band splitting under the action of strain has to be considered in order to calculate the optimum doping and the injected carrier density.

The most important technical situations are given by a Ge (or GeSn) under tensile strain (Fig. 12.10), by unstrained GeSn (Fig. 12.11), and by compressive strained GeSn (Fig. 12.12). As mentioned above the tensile strain reduces $\Delta E_c$ and it splits the valence band, with the lh band on top (Fig. 12.10) and the hh band below ($\delta E_v$ at the BZ center at $\vec{k} = 0$). The necessary tensile strain for a crossover to a direct semiconductor is high, about 2%–5%, but in detail depending on the strain direction (uniaxial, biaxial) and the assumed deformation potential parameters. Unstrained GeSn enhances the lattice constant, reduces the bandgap $E_{\text{gdir}}$ and the difference $\Delta E_c$, and does not lift the degeneracy of lh and hh valence bands (Fig. 12.11). The crossover to a direct semiconductor takes place at about 8% Sn content. Technical handling and strain management in GeSn are limited by its low temperature fabrication window. Therefore, often devices with GeSn in compressive strain are fabricated. These device structures need higher Sn content for $\Delta E_c$ reduction and the hh band is on top of the valence band structure (Fig. 12.12).

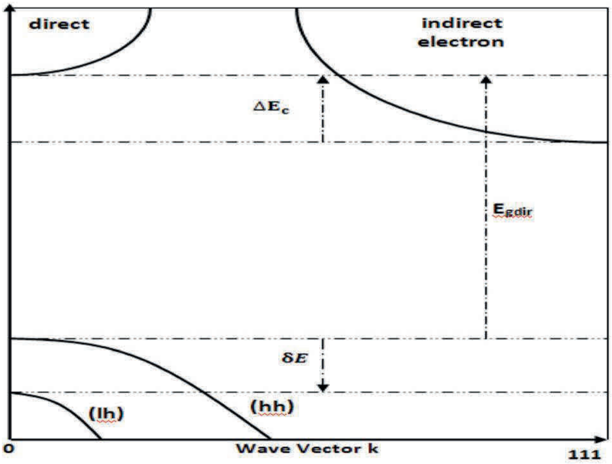

**Figure 12.12** Band structure of compressive stained GeSn.

### 12.6.1 Injected Carrier Densities and Layer Doping

From the requested quasi-Fermi energies $F_c$ and $F_v$ one can undoubtedly derive the minimum carrier levels $n$ and $p$ for gain $g = 0$. From these we can calculate the recommended doping level for the condition of minimum injected carrier densities $\Delta n$ and $\Delta p$.

Key parameters for the carrier levels are the energy difference $\Delta E_c$ between the indirect conduction band edge and the direct one (Fig. 12.10) and the energy difference $\delta E_v$ between the hh and the lh bands. The electron concentration is determined by the parameter $\Delta E_c$ and the hole concentration $p$ by the parameter $\delta E_v$. The energy difference $\Delta E_c$ is a function of Sn and strain, whereas the lh-hh energy difference $\delta E_v$ is a function of strain alone.

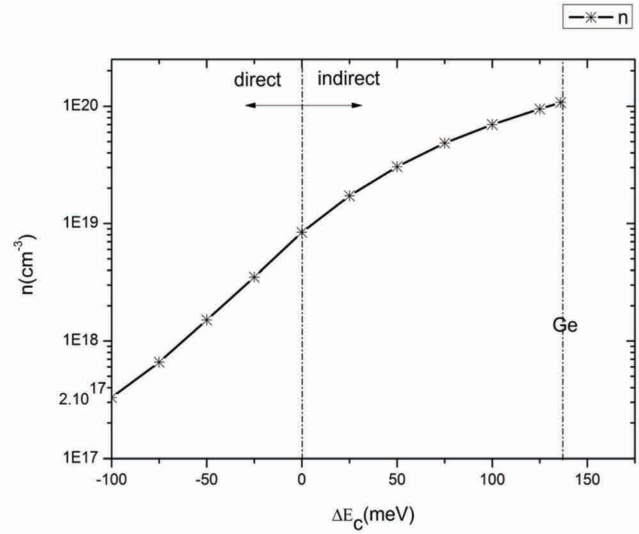

**Figure 12.13** The necessary electron concentration n to obtain occupation inversion with gain $g = 0$, given as a function of the direct/indirect gap $\Delta E_c$.

Figure 12.13 shows the dependence of the electron concentration $n$ on the energy difference $\Delta E_c$. The numerical values are obtained with the material parameters of Ge, but the general trend is independent of that. The necessary concentration of electrons is very high (about $10^{20}/\text{cm}^3$) for unstrained Ge ($\Delta E_c = 136$ meV) and drops down to yet higher values (about $10^{19}/\text{cm}^3$) at the direct/

indirect band crossover ($\Delta E_c = 0$), and it continues to decrease to direct bandgap regime ($\Delta E_c < 0$) with a low saturation level (about $10^{17}/\mathrm{cm}^3$) for a strong direct semiconductor behavior ($\Delta E_c < -150$ meV).

Figure 12.14 shows the dependence of the hole concentration $p$ on the energy difference $\delta E_v$. Note, we use positive values of $\delta E_v$ for tensile strain (lh sub-band above hh sub-band at wave vector $\vec{k} = 0$) and negative values for compressive strain. The hole concentration for compressive strain and unstrained material is moderately high (about $3\cdot 10^{18}/\mathrm{cm}^3$), and it drops sharply down to a lower level with tensile strain reaching a saturation (about $2\cdot 10^{17}/\mathrm{cm}^3$) at strong tensile strain ($\delta E_v > 125$ meV).

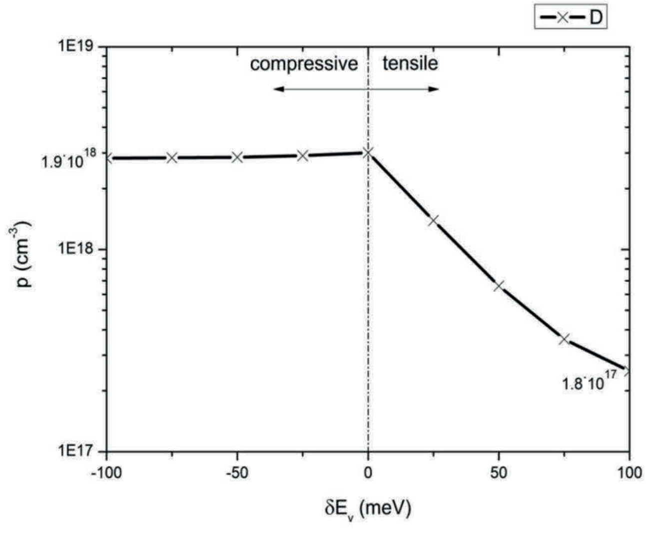

**Figure 12.14** The necessary hole concentration $p$ (for $g = 0$) given as a function of the strain related lh-hh energy gap $\delta E_v$.

What are the consequences of the data in Figs. 12.13 and 12.14 for the optimum doping and carrier injection levels? The electron concentration in the indirect semiconductor regime ($\Delta E_c > 0$) is always considerably higher than the hole concentration. This means the carrier injection level is given by the requested $p$ concentration whereas the much higher electron concentration is mainly provided by the higher n-doping $N_D$, which ranges from $10^{20}/\mathrm{cm}^3$ for unstrained Ge to about $5\cdot 10^{18}/\mathrm{cm}^3$ for the indirect/direct crossover material (either obtained by Sn alloying or a tensile strain or a combination of both). The minimum injection carrier density $\Delta n = \Delta p$ is given by the requested hole density, and it depends on the strain splitting of both hole sub-bands. The injected carrier density ranges from about $3 \cdot 10^{18}/\text{cm}^3$ for compressive and unstrained material to $2 \cdot 10^{17}/\text{cm}^3$ for highly tensile strained material. Therefore, we see two beneficial effects of the tensile strain within the indirect bandgap regime, the n-doping level is lower compared with the unstrained material because of a lower $\Delta E_c$ and the injected carrier density is lower because the minimum $\Delta n = \Delta p = p$ decreases by a factor of 15 with high tensile strain. The situation seems to be more complex in the direct semiconductor regime because the necessary $n$ and $p$ values cover similar ranges from several $10^{18}/\text{cm}^3$ to $10^{17}/\text{cm}^3$ so that theoretically a p-doping could be necessary for compressive strained and unstrained material with $\Delta E_c < -25$ meV. In practice a compressive strained Sn needs very high Sn contents to obtain a direct semiconductor state, which is technically complex and not very favorable for an Si-based device. For unstrained GeSn, we see an undoped GeSn as optimum (n=p) for a slight direct GeSn (around a difference = –25 meV) and we recommend a slight p-doping in the $10^{17}$–$10^{18}/\text{cm}^3$ range for more direct GeSn alloys. Details of the influence of Sn and strain $\varepsilon$ on the band parameters $\Delta E_c$ and $\delta E_v$ are given in Chapter 11. Here we need only rough values to sketch the general trends. For this reason we simplify the Sn influence by a linear function with a direct/indirect crossover at about 8% Sn. Then with about 1.5% Sn increase the direct band approaches by 25 meV, for example, with 6% Sn it is an indirect semiconductor ($\Delta E_c \approx +35$ meV) and with 10.5% it is a direct one ($\Delta E_c \approx -40$ meV). Tensile strain reduces the energy gap $\Delta E_c$ between direct band and indirect one. For a first assessment, a linear dependence on strain may be assumed. The valence band splitting $\delta E_v$ can only be treated linearly at small strain values because the hh sub-band moves linearly with strain but the lh follows a square root law [27]. Around 5% uniaxial strain and around 2% biaxial strain are needed to get a crossover of direct and indirect conduction bands [28].

Tensile-strained GeSn (containing about 10% Sn) with low doping levels would fulfill demands for low injection and low carrier concentration because the sub-bands defining the band properties—the direct conduction band and the lh valence band—both need low concentrations of carriers for population inversion.

### 12.6.2 Internal Quantum Efficiency and Threshold Current

The electrically stimulated semiconductor laser is the most relevant laser type for applications. The crucial parameters for the electrical operation are the threshold current $I_{\mathrm{th}}$ for the onset of laser emission. This threshold requires a positive net gain $G$ ($G > 0$). In the section before, we have seen that the gain is correlated with the necessary carrier densities in the active medium. In this part, the connection between injection currents and carrier densities is given for idealized carrier confinement conditions. On this basis the internal quantum efficiency (IQE) may be treated as a competition between radiative and nonradiative recombination processes. The simplest electrical laser structure consists of a p/n junction diode. Here, the injected current induces a deviation from the equilibrium that reaches more than a diffusion length $L_{\mathrm{d}}$ apart from the junction. Carrier confinement is obtained very effectively by a heterostructure [12]. For a Ge-based laser, larger bandgap materials, such as Si [29] and GeSiSn [30], may be utilized as barrier materials, for example, for a Si/Ge/Si double heterobarrier structure. The injection efficiency for such a heterostructure carrier confinement structure is ideally assumed to be perfect, 100% [29], which means all the injected carriers are provided within the active layer for recombination, radiative and nonradiative. The IQE is defined under these idealizing conditions as the ratio between radiative recombination rate $U_{\mathrm{rad}}$ and total recombination rate, which is written as the sum of $U_{\mathrm{rad}}$ and nonradiative recombination rate $U_{\mathrm{nrad}}$.

$$\mathrm{IQE} = \frac{U_{\mathrm{rad}}}{U_{\mathrm{rad}} + U_{\mathrm{nrad}}} \tag{12.44}$$

In unstrained Ge, the radiative recombination rate $U_{\mathrm{rad}}$ is already dominated by the direct transition between the Γ minimum in the conduction band and the valence band. The dominance of direct radiative recombination in comparison with the indirect one will be even larger with reduced $\Delta E_{\mathrm{c}}$ in GeSn and strained Ge. Earlier observations of comparable indirect and direct emissions from substrate or thick layers were explained by self-absorption of the more energetic direct emission [31]. The radiative recombination rate is given by

$$\left(\frac{n_{\mathrm{dir}}}{n}\right) pU_{\mathrm{rad}} = R_{\mathrm{dir}} . n_{\mathrm{dir}} = R_{\mathrm{dir}} n, \tag{12.45}$$

with $R_{\mathrm{dir}}$ the recombination rate for direct recombination. It is proportional to the concentration of the direct electrons $n_{\mathrm{dir}}$ and of holes. The competing nonradiative recombination is dominated by the acceleration of electron-hole annihilation at midgap recombination centers (Shockley–Read–Hall [SRH] effect) and by Auger recombination. In an n-type semiconductor both these effects contribute to $U$ as

$$U_{\mathrm{nrad}} = \frac{p}{\tau_{\mathrm{SRH}}} + C_{\mathrm{n}} n^2 p. \tag{12.46}$$

The recombination at the mid-bandgap center is described by the minority carrier life time $\tau_{\mathrm{SRH}}$, which is smaller in a semiconductor with defects. Defects may be dislocations, vacancies or interstitials, and metallic contaminations. These defects can be easily produced by a lattice mismatch, nonequilibrium growth conditions, and improper device processing. Especially the Saraswat group [32] has addressed the importance of high-quality active layers with a long minority carrier lifetime for Ge-based lasers with good IQE. At very high carrier concentrations the Auger effect dominates because of its quadratic dependence on the electron concentration (in n-material). In an Auger process two electrons with opposite momentums meet a hole with zero momentum and they can therefore recombine without the help of a phonon. The defect-related minority carrier lifetime and the Auger recombination may be combined to a concentration-dependent total nonradiative lifetime for which the following relation holds:

$$\frac{1}{\tau_{\mathrm{nrad}}} = \frac{1}{\tau_{\mathrm{SRH}}} + C_{\mathrm{n}} n^2 \tag{12.47}$$

Figure 12.15 shows the resulting inverse nonradiative lifetime $\left(\frac{1}{\tau_{\mathrm{nrad}}}\right)$ as a function of the electron concentration in a double logarithmic presentation with the defect-related lifetime as a parameter. The Auger recombination coefficient at room temperature is chosen as $10^{-30}$ cm$^6$/s [33]. The defect-related minority carrier lifetime varies between below 1 ns for a material with high dislocations and point defect densities (named "bad material" here) and much more than 100 ns (good material) for materials with low defect densities. The Auger process dominates the recombination at very high electron concentrations ($10^{20}/\text{cm}^3$). Then even a good material has high nonradiative recombination rates. The advantages of good materials (with respect to lifetime) are only visible at lower electron levels ($10^{19}/\text{cm}^3$), which are obtained in laser structures with highly strained Ge or GeSn with above 5% Sn.

The IQE is computed by combining Eqs. 12.44–12.46.

$$\text{IQE} = \frac{R_{\text{dir}} n (n_{\text{dir}} / n)}{1/\tau_{\text{SRH}} + C_{\text{n}} n^2}. \tag{12.48}$$

This relation is also valid for the LED regime if the perfect carrier confinement is fulfilled.

A high defect recombination rate (low SRH lifetime $\tau_{\text{SRH}}$) reduces the quantum efficiency of emission, which is intuitively clear as a nonradiative channel is opened. But a low lifetime also influences the threshold current $I_{\text{th}}$, which is necessary to establish the carrier levels requested for a positive net gain $G$.

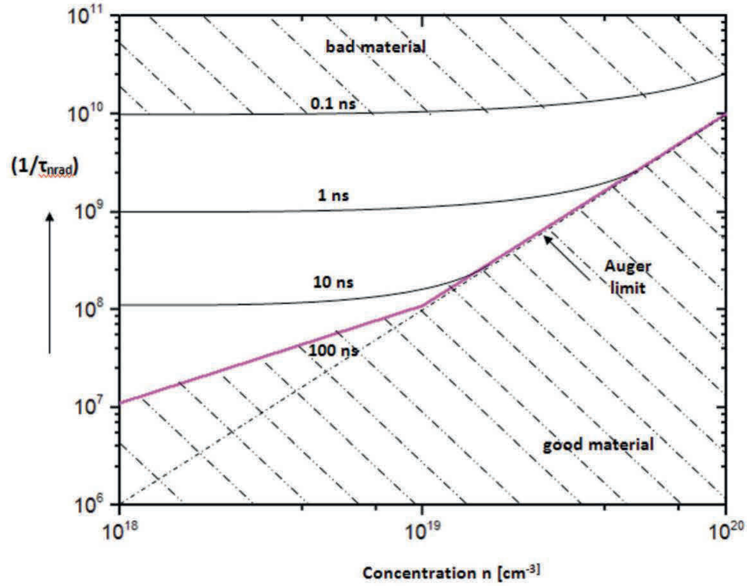

**Figure 12.15** Dependence of the inverse of nonradiative lifetime ($1/\tau_{\text{nrad}}$) from the electron concentration n for different defect-related lifetimes $\tau_{\text{SRH}}$.

Let us assume some conditions as for quantum efficiency calculations, which means perfect carrier confinement and n-doping of the active layer. The continuous loss of carriers by the recombination has to be counterbalanced by the injected carrier of the electrical current.

$$I = J.A = qV(U_{\text{rad}} + U_{\text{nrad}}), \tag{12.49}$$

where $I$ is for current, $J$ for current density, $A$ for cross section, $V$ for volume, and $U$ for recombination rate (per volume).

With $V = A \cdot d$ ($d$ is the thickness of the confinement region) we use Eqs. 12.45, 12.46, and 12.49 to obtain

$$J_{\text{th}} = q^* p_{\text{th}} \left( R_{\text{dir}} n_{\text{dir}} + 1/\tau_{\text{SRH}} + C_{\text{n}} n_{\text{th}}^2 \right) \tag{12.50}$$

if $p_{\text{th}} = \Delta n = \Delta p$ and $n_{\text{th}} = N_{\text{D}} + p_{\text{th}}$ are set to the values needed for the net gain $G = 0$. Please remember that we have given in the last section a recipe for the optimum choices of doping and carrier densities to get the gain $g = 0$. The injected carrier densities required to get the net gain $G > 0$ are higher because the modal confinement ($\Gamma \leq 1$) and the extinction coefficient $\alpha'$ request a positive gain $g_{\text{th}}$ to obtain a net gain $G = 0$ (see Eq. 12.20). A general rule for the choice of $\Gamma$ and $\alpha'$ is not available because these parameters depend on the device design. The extinction coefficient $\alpha'$ contains device-specific components such as absorption from contact layers and surface scattering, but also an unavoidable component from free carrier absorption (the fundamental spontaneous absorption of the active layers is contained already in the gain definition and must not be added here).

The strong increase of the nonradiative recombination at high doping and carrier injection levels causes very high threshold currents $I_{\text{th}}$. For example, a threshold current density of 500 kA/cm$^2$ is necessary for a doping of $10^{20}$/cm$^3$ and a carrier injection of $10^{19}$/cm$^3$. The threshold current density shrinks to 5 kA/cm$^2$ for a doping of $10^{19}$/cm$^3$ and a carrier injection of $5 \cdot 10^{18}$/cm$^3$. The Auger limit restricts continuous wave (CW) operation of Ge-based laser to strain and alloy conditions, which reduces the direct/indirect gap $\Delta E_{\text{c}}$ to below 100 meV and increases the lh-hh valence band splitting to above 0 meV.

## 12.7 Experiments

Direct bandgap semiconductors mostly from III/V compounds dominate the market for visible and infrared lasers of compact size and moderate power output. They use direct bandgap emission very efficiently. The low radiative emission rate of the indirect semiconductor silicon prohibited the use of the bulk silicon as an active laser medium. The silicon-based research community put a lot of effort to overcome the low radiative emission rate by different types of nanostructuring, by introducing defect levels, and by doping with color centers (rare earth elements). All this effort brought rich physical understanding and an enhancement of radiative emission but failed to push silicon as a laser material. The general opinion that an indirect semiconductor is useless for laser emission seemed to be confirmed. However, the situation with Ge is quantitatively very different from the viewpoint of the energy distance $\Delta E_c$ between the lower indirect band and the higher lying direct band. This energy difference $\Delta E_c$ is very high for Si (more than 2 eV, which is more than 80 kT at room temperature) but moderately small (0.0136 eV, which is about 5 kT at room temperature) for Ge. There were some rumors in the Western world that a Russian researcher had achieved gains in n-doped Ge but made no laser demonstration. Probably, the first group that spent continuous theoretical and experimental efforts for a Ge laser was the Kimerling group [34, 35] at MIT, USA. They calculated the gain spectrum $g$ $(hv)$ of n-doped Ge for different injection carrier levels $\Delta n = \Delta p$ and they found rather high gain values for a population inversion factor $(f_c - f_v) = 1$. Their approach is based on the inherent connection between stimulated emission and absorption (Eq. 12.5) and on the joint density of states model (Eq. 12.13) with a reduced carrier mass $m_r$ (Eq. 12.2). The population inversion factor $(f_c - f_v)$ connects stimulated emission with the absorption coefficient

$$g(hv) = \alpha_{\text{dir}}(f_c - f_v) \tag{12.51}$$

with $\alpha_{\text{dir}}$ as the absorption coefficient connected to the direct bandgap transition. That is easily demonstrated by switching the population inversion factor from equilibrium $(f_c - f_v) = -1$ to lasing conditions $1 > (f_c - f_v) > 0$. At equilibrium the gain $g$ is $-\alpha$ (loss). This condition (Eq. 12.51) allows the calculation of the gain spectrum from the absorption coefficient and the quasi-Fermi levels $F_c$ and $F_v$. The absorption coefficient $\alpha_{\mathrm{dir}}$ may be acquired by a transmission experiment or from the known energy relation of direct absorption processes. Note that near the direct bandgap three absorption processes take place: the searched direct absorption, the indirect band absorption, and the free carrier absorption. The direct band-to-band absorption can be theoretically calculated by solving the electron-photon scattering in a crystalline potential [36, 37].

$$\alpha(hv) = \frac{q^2 hc\mu_0}{2m_0^{\ 2}} \frac{\rho_{\mathrm{cv}}}{n_{\mathrm{r}}} \frac{1}{g(hv)} Z_{\mathrm{j}}, \tag{12.52}$$

where $q$, $h$, $c$, $\mu_0$, $m_0$, and $n_{\mathrm{r}}$ have the usual meaning (electron charge, Planck's constant, speed of light, permittivity coefficient, free electron mass, and refractive index, respectively) and $\rho_{\mathrm{cv}}$ and $Z_{\mathrm{j}}$ are the transmission matrix element and joint DOS, respectively.

The joint DOS of $Z_{\mathrm{j}}$ is given within the effective mass model as

$$Z_{\mathrm{j}} = 2\pi\left(\frac{2m_{\mathrm{r}}}{h^2}\right)^{3/2}\left(hv - E_{\mathrm{g\Gamma lh}}\right)^{1/2}, \tag{12.53}$$

with the reduced mass $m_{\mathrm{r}}$ (Eq. 12.12). The absorption near the direct band edge may be simplified described by

$$\alpha(hv) = \frac{A\left(hv - E_{\mathrm{g\Gamma lh}}\right)^{1/2}}{hv} \tag{12.54}$$

if we combine all slowly varying properties into a constant $A$. The constant $A$ for Ge is about

$$2.10^4\ \mathrm{eV}^{1/2}/\mathrm{cm}$$

The more experienced reader may notice that we did not discuss the influence of excitons on the emission/absorption spectrum. The influence of excitons is treated in textbooks on optical properties [36] and in a recent publication of the Menendez group [38].

We continue with the simplified treatment of the band-to-band transition.

The absorption edge of tensile-strained Ge moves toward lower energy because of the shrinkage of the direct bandgap. Since the lh or hh band separate under strain, two optical transitions make up the total absorption. Then, the absorption of tensile-strained Ge is

$$\alpha(hv)=\frac{A}{h\vartheta}\left[k_1\left(hv-E_{\mathrm{grlh}}\right)^{1/2}+k_2\left(hv-E_{\mathrm{grhh}}\right)^{1/2}\right], \qquad (12.55)$$

where $k_1$ and $k_2$ are coefficients attributed to the contributions from different reduced masses.

$$k_1=\frac{m_{\mathrm{rlh}}^{3/2}}{(m_{\mathrm{rlh}}^{3/2}+m_{\mathrm{rhh}}^{3/2})}$$

$$k_2=\frac{m_{\mathrm{rhh}}^{3/2}}{(m_{\mathrm{rlh}}^{3/2}+m_{\mathrm{rhh}}^{3/2})}$$

$$k_1+k_2=1$$

For Ge the normalized coefficients $k_1$ and $k_2$.are given as 0.68 and 0.32, respectively.

The calculated gain spectrum of an n-Ge ($N_D$ = 7 × $10^{19}/\mathrm{cm}^3$) under slight tensile strain (0.25%) is shown in Fig. 12.16. High n-doping of unstrained or slightly strained Ge is necessary to get the electron quasi-Fermi level toward the direct band edge.

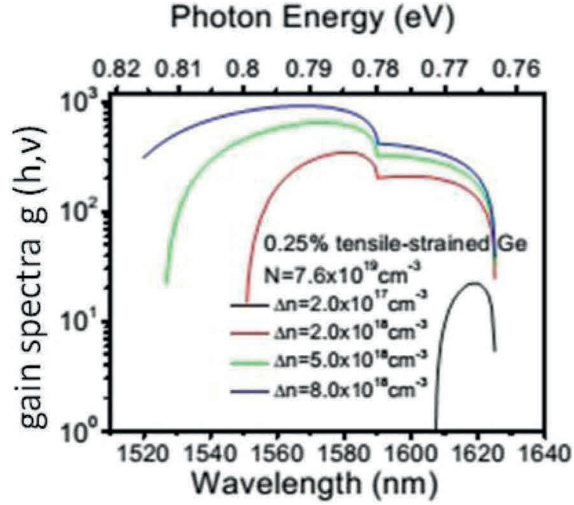

**Figure 12.16** Gain spectra g(hv) from the direct transition in 0.25% tensile-strained n$^+$-Ge with $N$ = 7.6 × $10^{19}$ cm$^{-3}$ at different injected carrier densities. Reprinted with permission from Ref. [35] © The Optical Society.

The injected carrier density is necessary to push the hole quasi-Fermi level toward the valence band. A positive gain is obtained from an injection level of $5 \cdot 10^{17}/\text{cm}^3$ ($\Delta n = \Delta p$) but the gain is small (50/cm$^2$) and restricted to a small band above the band edge (which is 0.7 eV for the assumed strain level). With higher injection levels the gain increases to about 1000/cm$^3$ for $\Delta n = \Delta p = 8 \cdot 10^{18}/\text{cm}^3$. Clearly visible in the gain spectrum is the overlay of the separated lh and hh contributions where the quasi-Fermi level touches the bottom of the hh sub-band. Optical gain in a material under injection does not necessarily lead to a laser emission that requires the optical gain to overcome all kinds of optical losses. An unavoidable kind of loss is caused by the free carrier absorption within a band. The free carrier absorption increases with wavelength and becomes significant at higher carrier densities. An optimistic assessment of the lasing potential assumes that the optical confinement is perfect ($\Gamma = 1$) and the losses are caused by the free carrier absorption. Then the net gain $G$ reduces simply to

$$\Gamma g - \alpha' = g - \alpha_{\text{fc}}, \tag{12.57}$$

with $\Gamma$ as the optical confinement factor, $g$ as the gain (a sum of all extinction losses except the fundamental absorption), $\alpha_{\text{fc}}$ as the free carrier absorption coefficient. The free carrier absorption scales with the carrier concentration and with the square of the wavelength (Drude model). A fit of experimental data [35] at room temperature results in

$$\alpha_{\text{fc}}(\lambda) = -3.4 \cdot 10^{-25} n\lambda^{2.25} - 3.2 \cdot 10^{-25} p\lambda^{2.43}, \tag{12.58}$$

where $\alpha_{\text{fc}}$ is measured in units of cm$^{-1}$, $n$ and $p$ are measured in units of cm$^{-3}$, and $\lambda$ is measured in units of nm. The free hole absorption is higher than the free electron absorption, roughly 4 times higher at a wavelength of 2 µm. At this wavelength an optical gain of 1000/cm exceeds the free carrier absorption up to $1.11 \cdot 10^{20}$ electrons but only up to $3 \cdot 10^{19}$ holes. The conditions for Ge lasing with many more electrons than holes benefit from the lower free electron absorption.

The technical realization of such a laser needs good optical confinement, low losses from surface scattering, and good electrical confinement for threshold current reduction. Figure 12.17 shows a device suggestion [34] from the Kimerling group.

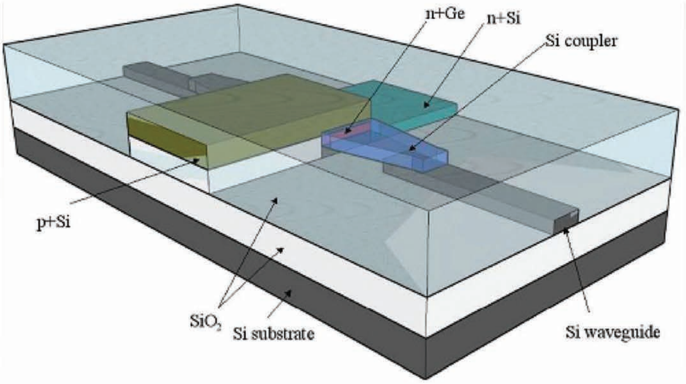

**Figure 12.17** Proposed schematic of the integration of a Ge laser with a Si waveguide. Reprinted from Ref. [34] with permission from the Massachusetts Institute of Technology ("MIT").

A silicon-on-insulator (SOI) substrate gives Si waveguides with good optical confinement. The waveguide is connected to the laser device by a tapered Si coupler. The laser device itself is composed of an n$^+$-Si/n-Ge/p$^+$-Si double heterostructure (DH) with good carrier confinement.

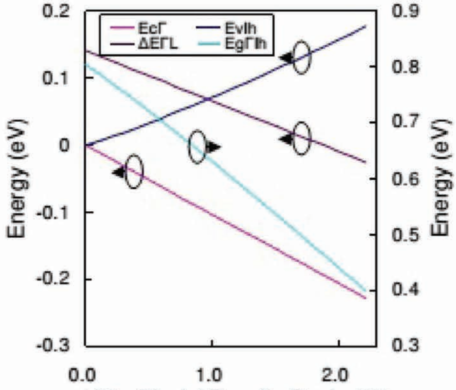

**Figure 12.18** Strain dependency of Ge direct bandgap $E_{g\Gamma lh}$ (energy scale on the right). The energy scale on the left is valid for the conductance band Γ to L valley separation $\delta E = E_{\Gamma L}$, the lh valence band edge $E_{Vlh}$, and the direct conductance band edge $E_{C\Gamma}$, $E_{C\Gamma G}$ and $E_{Vlh}$ are plotted with respect to their unstrained positions. Reprinted with permission from Ref. [39] © The Optical Society.

Liu et al. [35] calculated with the above-given data the net gain $G$ for a bulk n$^+$-Ge ($N_D = 1 \times 10^{20}/\text{cm}^3$) under tensile strain ($\varepsilon = 0.25\%$). The bulk Ge needs higher doping ($10^{20}/\text{cm}^3$) and higher injection ($\Delta n = 1 \times 10^{19}$) compared to slightly strained Ge with $N_D = 7 \times 10^{19}/\text{cm}^3$ and $\Delta n = 3.5 \cdot 10^{18}/\text{cm}^3$ in order to get a positive net gain $G$. Wada et al. [39] suggested micromechanical methods to increase the tensile strain level. Figure 12.18 shows the bandgap parameter as a function of biaxial strain.

### 12.7.1 Experimental Verification of Laser Light Emission from Group IV Materials

In Table 12.1, three different main configurations for laser in Si-based photonic systems are defined:

- Monolithic integration with Si photonics
- Hybrid mounting of group III/V laser on Si photonic systems
- Light coupling from an external laser source

All these system configurations have their own pros and cons, but their maturity differs greatly. Light coupling from an external source is now a de facto standard that will be partly replaced in the future by hybrid and monolithic approaches. Hybrid approaches use the well-developed III/IV lasers. Si photonics–based efforts are mainly concerned with mounting or bonding techniques for evanescent coupling of the light wave from the top-lying thinned laser to the Si-based waveguide below [9, 10, 40–44]. The details of the laser structure, the thinning procedure, the bonding, and the III/V laser for Si waveguide coupling schemes are sophisticated as, for example, explained in Ref. [42]. There, a quaternary InAlGaAs MQW laser is bonded to an SOI waveguide with a 500 nm device layer on a 1 μm thick buried oxide. The 1.5 μm wide silicon waveguide was defined by etching, as also the first-order grating on the Si waveguide, to create the resonator for the distributed feedback (DFB) laser. A DFB laser diode is a good candidate for the light source in wavelength division multiplexing systems. Single-frequency emission, short cavity length (100–200 μm), moderate threshold current density (1.1 KA/cm$^2$), and high-speed direct modulation (12.5 Gb/s) were reported. This work is used as a reference for comparing the efforts with monolithically integrated laser variants. The monolithic laser variants target in two directions with either III/V epitaxy on the substrate or group IV materials with strained Ge and GeSn. III/V epitaxy is a good choice for the laser part [45, 46] because of the excellent understanding of laser action and good optical gain, but the acceptance and frequent use of III/V materials with Si technology remain an open question. Electrically stimulated group IV lasers on Si could fill the gap in monolithically integrated photonic systems despite their imperfect performance in realized lasers [47]. Promising work for Ge-on-Si lasers was done by the MIT group of Kimerling et al. They demonstrated first [11] in 2010 an optical stimulation and two years later (2012) an electrical stimulation of a Ge laser on Si [12]. As the active laser material they used n-doped Ge with a slight tensile strain ($\varepsilon = 0.2\%$). The slight tensile strain was simply produced by annealing the Ge-on-Si laser to temperatures above 750°C. The thermal expansion mismatch causes the slight strain in the before-strain-relaxed Ge. This experimental proof was important not only for the technical development of on-chip lasers but also for clarification of a basic discussion on the possible net gain in Ge. Carroll et al. [48] doubted that the gain in Ge can overcome the fundamental losses, and they concluded from pump probe experiments that the losses are much higher than the usually assumed free carrier absorption. Koerner et al. [49] confirmed the experimental finding of the MIT group by even driving an unstrained Ge laser to the then very high (500 kA/cm$^2$) threshold current density. High tensile strain and alloying with Sn should reduce the threshold current density. Wirths et al. [50] demonstrated the fundamental use of GeSn as the active gain material with optical excitation at low temperatures. Here, progress in the synthesis of metastable GeSn alloys by epitaxy should deliver room temperature lasers with low threshold current and shift of the emission wavelength from the telecommunication wavelength 1.55 μm toward the midinfrared (2–3 μm) wavelength. Table 12.7 gives a comparison of different group IV laser realizations and two group III/V lasers as references.

The status of group IV heterostructure lasers depends strongly on progress in the synthesis of metastable materials with defined strain values [51]. This can easily be seen by looking at the room temperature operation of these lasers. The basically hardest conditions are given by the very high electron densities of unstrained or slightly strained Ge, whereas the lower separation by the indirect-direct bandgap energy $\Delta E_c$ in highly strained Ge or GeSn requests much lower carrier injection levels. However, the experimental status reflects exactly the maturity of the material preparation and process stability, with the slightly strained Ge in the leading position.

**Table 12.7** A selection of monolithic heterostructure lasers on Si

| Active material | Direct semi-conductor | Wavelength (µm) | Electron stimu-lation | RT operation | Single laser line | CW | Ref. |
|---|---|---|---|---|---|---|---|
| GaInAlAs MQW | + | 1.55 | + | + | + | + | [42] |
| InAs, QD | + | 1.3 | – | + | + | + | [45] |
| n-Ge, unstrained | – | 1.7 | + | + | – | – | [49] |
| n-Ge, strained | — | 1.6 | — | + | — | — | [11] |
| n-Ge, strained | — | 1.6 | + | + | + | — | [12] |
| GeSn | + | 2.3 | — | — | — | — | [50] |

*Note*: For comparison a hybrid laser on Si [42] is added.

## 12.8 Summary and Outlook

The lack of efficient Si light sources seemed to limit the applicability of Si-based photonics. Within a decade a variety of solutions have either already overcome or show the potential to overcome the small bottleneck in Si photonics. Solutions range from external light sources that couple their light via fiber in the chip, to hybrid lasers mounted on the chip, to a bundle of monolithic integration techniques (including III/V semiconductors and group IV semiconductors). The first two solutions offer good performances. Here the main focus is on production-friendly mounting techniques [52, 53]. The group IV lasers need the most intensive research efforts [41–62], with emphasis on strain, doping, Sn alloying, nanostructures, and epitaxy.

Excellent results were obtained for optically stimulated lasers at cryogenic temperatures [63–65]. High differential efficiencies

(<50%) were obtained with strained Ge microbridges [63]. The high strain of 5.4%–5.9% shifts the emission wavelength in the mid-IR region (3.2–3.7 µm). Lasing persists up to 100 K. Lasing persists nearly up to room temperature by combining GeSn alloys with high strain values [64]. Using tensile-strained microdisc GeSn resonators, low optical threshhold densities of about 1 kW/cm$^2$ could be obtained [65], allowing continuous wave operation up to 70 K. Obtaining room-temperature operation and electrical stimulation [66] of the laser will be dominant challenges for group IV laser research within the next few years.

## References

1. N. Koshida (2007). Luminescence and related properties of nanocrystalline porous silicon, in *Landolt-Boernstein*, *New Series*, Vol. III, 34C3, Semiconductor Quantum Structures-Optical Properties (Springer-Verlag).
2. E. Kasper, H.-J. Herzog and H. Kibbel (1975). A one-dimensional SiGe superlattice grown by UHV epitaxy, *Appl. Phys.*, **8**, 199.
3. L. T. Canham (1990). Silicon quantum wire array fabrication by electrochemical and chemical dissolution of wafers, *Appl. Phys. Lett.*, **57**, 1046.
4. L. Pavesi, L. Dal Negro, C. Mazzoleni, G. Franzo and F. Priolo (2000). Optical gain in silicon nanocrystals, *Nature*, **408**, 440.
5. U. Gnutzmann and K. Clausecker (1974). Theory of direct optical transitions in an optical indirect semiconductor with a superlattice structure, *Appl. Phys.*, **3**, 9.
6. H. Brugger, G. Abstreiter, H. Jorke, H. J. Herzog and E. Kasper (1986). Dispersion of folded phonons in superlattices, *Phys. Rev. B*, **33**, 5928.
7. R. Zachai, K. Eberl, G. Abstreiter, E. Kasper and H. Kibbel (1990). Photoluminescence in short-period Si/Ge strained layer superlattices, *Phys. Rev. Lett.*, **64**, 1055.
8. H. Presting, U. Menzcigar and H. Kibbel (1993). Electro- and photoluminescence studies from ultrahin SimGen superlattices, *J. Vac. Sci. Technol. B*, **11**, 1110.
9. B. Corbett, C. Bower, A. Fecioru, M. Mooney, M. Gubbings and J. Justice (2013). Strategies for integration of lasers on silicon, *Semicond. Sci. Technol.*, **28**, 094001.

10. A. W. Fang, B. R. Koch, R. Jones, E. Lively, P. Liang, Y. K. Kuo and J. E. Bowers (2008). A distributed Bragg reflector silicon evanescent laser, *IEEE Photonics Technol. Lett.*, **20**, 1667.
11. J. Liu, X. Sun, R. Camacho-Aguilera, L. C. Kimerling and J. Michel (2010). Ge-on-Si laser operating at room temperature, *Opt. Lett.*, **35**, 679–681.
12. Jr. E. Camacho-Aguilera, Y. Cai, N. Patel, J. T. Bassette, M. Romangnoli, L. C. Kimerling and J. Michel (2012). An electrical pumped Ge laser, *Opt. Express*, **20**, 11316.
13. H. C. Casey and M. B. Panish (1978). *Heterostructure Lasers: Fundamental Principles* (Academic Press, New York).
14. C. Weisbuch (1987). Optical properties of quantum wells, in *Physics and Applications of Quantum Wells and Superlattices*, E. E. Mendez and K. von Klitzing, eds., NATO ASI Series B170 (Plenum Press), pp. 261–299.
15. M. Asada, Y. Miyamoto and Y. Suematsu (1986). Gain and the threshold of three-dimensional quantum box lasers, *IEEE J. Quantum Electron.*, **QE-22**, 1915.
16. W. T. Tsang (1984). Heterostructure semiconductor lasers prepared by MBE, *IEEE J. Quantum Electron.*, **QE-20**, 1119.
17. Y. Arakawa and A. Yariv (1985). Theory of gain, modulation response and spectral linewidth in AlGaAs quantum well lasers, *IEEE J. Quantum Electron.*, **QE-21**, 1666.
18. G. Mak and H. M. van Driel (1994). Femtosecond transmission spectroscopy at the direct band edge of germanium, *Phys. Rev. B*, **49**, 16817.
19. X. Q. Zhou, H. M. van Driel and G. Mak (1994). Femtosecond kinetics of photoexcited carriers in germanium, *Phys. Rev. B*, **50**, 5226.
20. S. A. Claussen, E. Tasyurek, J. E. Roth and D. A. B. Miller (2010). Measurement and modeling of ultrafast carrier dynamics and transport in germanium/silicon-germanium quantum wells, *Opt. Express*, **18**, 25596.
21. X. Wang, L. C. Kimerling, J. Michel and J. Liu (2013). Large inherent optical gain from the direct gap transition of Ge thin films, *Appl. Phys. Lett.*, **102**, 131116.
22. J. S. Blackmore (1982). Approximations for Fermi-Dirac integrals, *Solid State Electron.*, **25**, 1067.
23. S. M. Sze (1981). *Physics of Semiconductor Devices*, 2nd ed. (Wiley, New York).

24. E. Kasper, M. Oehme, J. Werner, T. Aguirov and M. Kittler (2012). Direct bandgap luminescence from Ge on Si pin diodes, *Front. Optoelectron.*, **5**, 256.
25. R. Neumann and G. Abstreiter (2000). Effective masses of electrons and holes in SiGe, in *EMIS Datareview Series*, Vol. 24 (INSPEC (IEE), London).
26. H. Kroemer (1978). The Einstein relation for degenerate carrier concentrations, *IEEE Trans.*, **ED-25**, 850.
27. E. Kasper and M. Oehme (2015). Germanium tin light emitters on silicon, *Jap. J. Appl. Phys.*, **54**, 04DG11.
28. R. Geiger, T. Zabel and H. Sigg (2015). Group IV direct bandgap photonics: methods, challenges and opportunities, *Front. Mater.*, **2**, 52.
29. J. Liu, R. Camacho-Aguilera, J. T. Bessette, X. Sun, S. Wang, Y. Cai, L. C. Kimerling and J. Michel (2012). Ge-on-Si optoelectronics, *Thin Solid Films*, **520**, 3354–3360.
30. G. Sun, R. A. Soref and H. H. Cheng (2010). Design of an electrically pumped SiGeSn/GeSn/SiGeSn double heterostructure mid-infrared laser diode, *Jpn. J. Appl. Phys.*, **108**, 033107.
31. T. Arguirov, M. Kittler, M. Oehme, N. V. Abrasimov, E. Kasper and J. Schulze (2011). Room temperature direct band gap emission from an unstrained Ge pin LED, *Solid State Phenom.*, **178**, 25.
32. D. S. Sukhdeo, S. Gupta, K. C. Saraswat, B. Dutt and D. Nam (2016). Impact of minority carrier lifetime on the performance of strained germanium light sources, *Opt. Commun.*, **364**, 233–237.
33. www.ioffe.ru/SVA/NSM/Semicond/Ge/Electronic.html
34. X. Sun (2009). Ge-on-Si light-emitting materials and devices for silicon photonics, PhD thesis, MIT.
35. J. Liu, X. Sun, D. Pan, X. Wang, L. C. Kimerling, T. L. Koch and J. Michel (2007). Tensile-strained, n-type Ge as a gain medium for monolithic laser integration on Si, *Opt. Express*, **15**, 11272.
36. P. Y. Yu and M. Cardona (1996). *Fundamentals of Semiconductors: Physics and Materials Properties* (Springer-Verlag, Berlin).
37. C. F. Klingshirn (2012). *Semiconductor Optics*, 4th ed. (Springer-Verlag, Berlin).
38. C. Xu, J. D. Gallagher, C. L. Senaratne, J. Menendez and J. Kouvetakis (2016). Optical properties of Ge-rich $Ge_{1-x}Si_x$ alloys: compositional dependence of the lowest direct and indirect gaps, *Phys. Rev. B*, **93**, 125206.

**39.** P. H. Lim, S. Park, Y. Ishikawa and K. Wada (2009). Enhanced direct bandgap emission in germanium by micromechanical strain engineering, *Opt. Express*, **17**, 16358.

40. S. Fathpour (2012). Emerging heterogeneous integrated platforms on silicon, *Nanophotonics*, **4**(1).

41. A. Spott, M. Davenport, J. Peters, J. Bovington, M. J. R. Heck, E. J. Stanton, I. Vurgaftman, J. Meyer and J. E. Bowers (2015). Heterogeneously integrated 2.0 µm CW hybrid silicon lasers at room temperature, *Opt. Lett.*, **40**, 1480.

42. C. Zhang, S. Srinivasan, Y. Tang, M. R. J Heck, M. L. Davenport and J. E. Bowers (2014). Low threshold and high speed short cavity distributed feedback hybrid silicon lasers, *Opt. Express*, **22**, 10202–10209.

43. H. T. Hattori, C. Seassal, E. Touraille, P. Rojo-Romeo, X. Letartre, G. Hollinger, P. Viktorovitch, L. Di Cioccio, M. Zussy, L. El Melhaoui and J. M. Fedeli (2006). Heterogeneous integration of microdisk lasers on silicon strip waveguides for optical interconnects, *IEEE Photonics Technol. Lett.*, **18**, 223.

44. S. Keyvaninia, C. Roelkens, D. Van Thourhout, C. Jany, M. Lamponi, A. L. Liepvre, F. Lelarge, D. Make, G. H. Duan, D. Bordel and J. M. Fedeli (2013). Demonstration of a heterogeneously integrated III-V/SOI single wavelength tuneable laser, *Opt. Express*, **38**, 5434.

45. Y. Wan, Q. Li, A. Y Liu, A. C. Gossard, J. E. Bowers, E. L. Hu and K. M. Lau (2016). Temperature characteristics of epitaxially grown InAs quantum dot micro-disk lasers on silicon for on-chip light sources, *Appl. Phys. Lett.*, **109**, 011104.

46. A. Y. Liu, C. Zhang, J. Norman, A. Snyder, D. Lubyshev, J. M. Fastenau, A. W. K. Liu, A. C. Gossard and J. E. Bowers (2014). High performance continuous wave 1.3 µm quantum dot laser on silicon, *Appl. Phys. Lett.*, **104**, 041104.

47. Z. Zhau, B. Yin and J. Michel (2015). On-chip light sources for silicon photonics, *Light Sci. Appl.*, **4**, e358.

48. L. Carroll, P. Friedli, S. Neuenschwander, H. Sigg, S.Cecchi, F. Isa, D. Chrastina, G. Isella, Y. Fedoryshyn and J. Faist (2012). Direct-gap gain and optical absorption in germanium correlated to the density of photo exited carrier, doping and strain, *Phys. Rev. Lett.*, **109**, 057402.

49. R. Koerner, M. Oehme, M. Gollhofer, M. Schmid, K. Kostecki, S. Bechler, W. Widmann, E. Kasper and J. Schulze (2015). Electrically pumped lasing from Ge Fabry-Perot resonators on Si, *Opt. Express*, **23**, 14815.

50. S. Wirths, R. Geiger, N. von den Driesch, G. Mussler, T. Stoica, S. Mantl, Z. Ikonic, M. Luysberg, S. Chiussi, J. M. Hartmann, H. Sigg, J. Faist, D. Buca and D. Grützmacher (2015). Lasing in direct-bandgap GeSn alloy grown on Si, *Nat. Photonics*, **9**, 88–92.
51. E. Kasper (2016). Group IV heteroepitaxy on Si for photonics, *J. Mater. Res.*, **31**, 3639–3649.
52. E. Kasper and V. Stefani (2008). Device with optical coupling window and fabrication method for this device, German patent, No. 102008051625 (in German).
53. J. Zhang, B. Haq, J. O'Callaghan, A. Gocalinska, E. Peluchi, A. J. Trinade, B. Corbette, G. Morthier and G.Roelkens (2018). Transfer-printing-based integration of a III-V-on-silicon distributed feedback laser, *Opt. Express*, **26**, 8821–8830.
54. B. Dutt, D. S. Sukhdeo, D. Nam, B. M. Vulovic, Z. Yuan and K. C. Saraswat (2012). Roadmap to an efficient germanium-on-silicon laser: strain vs. n-type doping, *IEEE Photonics J.*, **4**, 2002.
55. Z. Zhou, B. Yin and J. Michel (2015). On-chip light sources for silicon photonics, *Light Sci. Appl.*, **4**, e358.
56. Y. Cai, Z. Han, X. Wang, R. E. Camacho-Aguilera, L. C. Kimerling, J. Michel and J. Liu (2013). Analysis of threshold current behavior for bulk and quantum well germanium laser structures, *IEEE J. Sel. Top. Quantum Electron.*, **19**, 1901009.
57. D. Stange, S. Wirths, N. von den Driesch, G. Mussler, T. Stoica, Z. Ikonic, J. M. Hartmann, S. Mantl, D. Grützmacher and D. Buca (2015). Optical transitions in direct-bandgap $Ge_{1-x}Sn_x$ alloys, *ACS Photonics Lett.*, **2**, 1539–1545.
58. V. Reboud, et al. (2018). Optically pumped GeSn micro-disks with 16% Sn lasing at 3.1 μm up to 180 K, *Appl. Phys. Lett.*, **111**, 092101.
59. R. Loo, Y. Shimura, S. Ike, A. Vohra, T. Stoica, D. Stange, D. Buca, D. Kohen, J. Margetis and J. Tolle (2018). Epitaxial GeSn: impact of process conditions on material quality, *Semicond. Sci. Technol.*, **33**, 114010 (9pp).
60. N. von den Driesch, et al. (2018). Advanced GeSn/SiGeSn group IV heterostructure lasers, *Adv. Sci.*, **5**, 1700955.
61. P. O. Vaccaro, M. I. Alonso, M. Garriga, J. Gutiérrez, D. Peró, M. R. Wagner, J. S. Reparaz, C. M. Sotomayor Torres, X. Vidal, E. A. Carter, P. A. Lay, M. Yoshimoto and A. R. Goñi (2018). Localized thinning for strain concentration in suspended germanium membranes and optical method for precise thickness measurement, *AIP Adv.*, **8**, 115131.

62. G. Niu, G. Capellini, M. A. Schubert, T. Niermann, P. Zaumseil, J. Katzer, H.-M. Krause, O. Skibitzki, M. Lehmann, Y.-H. Xie, H. von Känel and T. Schroeder (2016). Dislocation-free Ge nano-crystals via pattern independent selective Ge heteroepitaxy on Si nano-tip wafers, *Sci. Rep.*, **6**, 22709.
63. F. T. Armand Pilon et al. (2019). Lasing in strained germanium microbridges, Nat. Commun., 10, 2724.
64. J. Chrétien et al. (2019). GeSn lasers covering a wide wavelength range thanks to uniaxial tensile strain, ACS Photon., 6, 2462–2469.
65. A. Elbaz et al. (2020). Ultra-low-threshold continuous-wave and pulsed lasing in tensile-strained GeSn alloys, Nat. Photon., arXiv:2001.04927.

66 Y. Zhou et al. (2020). Electrically injected GeSn lasers on Si operating up to 100 K, arXiv 2004.09402.